Title: Beta-arrestin 1 mediated Src activation via Src SH3 domain revealed by cryo-electron microscopy

Authors: Natalia Pakharukova[1,2], Brittany N. Thomas[1,2], Harsh Bansia[3], Linus Li[1], Rinat R. Abzalimov[3], Jihee Kim[1], Alem W. Kahsai[1], Biswaranjan Pani[1], Dana K. Bassford[1,2], Shibo Liu[3], Xingdong Zhang[1], Amedee des Georges[3,4,5]*, Robert J. Lefkowitz[1,2,6]*

Affiliations:

[1]Department of Medicine, Duke University Medical Center; Durham, NC 27710, USA.

[2]Howard Hughes Medical Institute, Duke University Medical Center; Durham, NC 27710, USA.

[3]Structural Biology Initiative, CUNY Advanced Science Research Center; New York, NY 10031, USA.

[4]Department of Chemistry and Biochemistry, City College of New York; New York, NY 10031, USA.

[5]Biochemistry and Chemistry PhD Programs, Graduate Center, City University of New York; New York, NY 10031, USA.

[6]Department of Biochemistry, Duke University Medical Center; Durham, NC 27710, USA.

*Corresponding author. Email: lefko001@receptor-biol.duke.edu, adesgeorges@gc.cuny.edu

Abstract: Beta-arrestins (βarrs) are key regulators and transducers of G-protein coupled receptor signaling; however, little is known of how βarrs communicate with their downstream effectors. Here, we use cryo-electron microscopy to elucidate how βarr1 recruits and activates non-receptor tyrosine kinase Src. βarr1 binds Src SH3 domain via two distinct sites: a polyproline site in the N-domain and a non-proline site in the central crest region. At both sites βarr1 interacts with the aromatic surface of SH3 which is critical for Src autoinhibition, suggesting that βarr1 activates Src by SH3 domain displacement. Binding of SH3 to the central crest region induces structural rearrangements in the β-strand V, finger, and middle loops of βarr1 and interferes with βarr1 coupling to the receptor core potentially impacting receptor desensitization and downstream signaling.

One-Sentence Summary: Beta-arrestin 1 uses two distinct sites to bind the SH3 domain of Src and drive relief of Src autoinhibition.

Main Text:

Beta-arrestins 1 and 2 (βarr1 and βarr2) are ubiquitously expressed scaffold proteins that interact with most, if not all, G-protein coupled receptors (GPCRs) (*1, 2*). βarrs mediate receptor desensitization and intracellular trafficking, as well as initiate downstream signaling cascades, independently or in concert with G-proteins (*3*). In their role as signal transducers, βarrs act as adaptor proteins that link GPCRs with numerous downstream effectors, including components of several mitogen-activated protein kinase cascades and Src family tyrosine kinases (*4-6*). Recent studies demonstrate that in addition to the scaffolding function, βarrs also directly allosterically activate effector enzymes, including non-receptor tyrosine kinase Src (*7, 8*), mitogen-activated

protein kinases c-Raf (*9*), and extracellular signal-regulated kinase 2 (*10*). However, the molecular mechanisms of βarr-mediated signal transduction remain unknown. Despite recent progress in obtaining several cryo-electron microscopy (cryo-EM) structures of GPCR–βarr complexes (*11-14*), there have been no structures of *βarr–effector* complexes. The main challenges arise from the transient nature of these complexes and the mid-micromolar affinity of their interactions necessitating additional stabilization techniques.

Src homology 3 (SH3) domains are one of the most ubiquitous binding modules with nearly 300 members found in the human genome (*15, 16*). SH3 domains recognize left-handed type II polyproline motifs; at present, there are several hundred structures of various SH3 domains complexed with polyproline-rich peptides. However, there are only a few structures of SH3 domains bound to a full protein or protein domain, including Nef from HIV-1, ubiquitin, and engulfment and cell motility protein 1 (ELMO1) (*17-23*). SH3-containing proteins are involved in various signaling pathways, such as cell growth and proliferation, endocytosis, and cytoskeleton remodeling (*24, 25*). A number of SH3-containing proteins were shown to interact with βarrs (*26*) potentially via one of the three polyproline binding motifs, two of which are located in the N-domain and the third one in the hinge region of βarr (*7*). Proto-oncogene kinase Src, the first discovered effector protein of βarrs, interacts with βarrs via its SH3 domain (*4, 7, 8, 27*), and the interaction is dependent on proline residues P88-P91/P120-P121 (βarr1 numbering used) (Fig. 1A) (*4, 7*). Earlier studies suggest that the interaction of βarr1 with SH3 drives allosteric activation of Src (*7, 8*). However, the molecular basis of Src recruitment and allosteric activation by βarrs remains elusive. Here we report the first high-resolution snapshots of βarr1 in complex with Src SH3 domain and three-domain Src (SH3-SH2-SH1, residues 83-533) by cryo-EM and elucidate the allosteric activation mechanism of Src kinase by βarr1.

βarr1 uses two distinct sites to bind SH3

To map the binding interface between the SH3 domain of Src and βarr1 we utilized a disulfide trapping strategy (*28*). We introduced cysteine substitutions at 18 different positions in βarr1 in proximity to P88-P91 and P120-P124 (Fig. 1A). Guided by the available structures of SH3 domains in complex with polyproline-rich peptides we designed 13 cysteine mutants of SH3 (Fig. 1B). We comprehensively tested 234 combinations of purified βarr1 and SH3 cysteine mutant pairs by inducing disulfide bond formation with hydrogen peroxide *in vitro*. Active βarr1 was shown to bind more strongly to SH3 (*8*), therefore, prior to disulfide trapping reactions βarr1 was activated using a synthetic phosphopeptide mimicking the C-tail of vasopressin 2 receptor (V2Rpp) and the stabilizing antibody fragment Fab30. Intriguingly, we observed the formation of the disulfide cross-linked SH3–βarr1–V2Rpp–Fab complexes by two βarr1 mutants, E92C and P120C, respectively (Fig. 1C, Fig. 1D). The SH3 mutant R95C in the RT-loop gave the strongest disulfide cross-linked band in both complexes, suggesting that SH3_R95 is in close proximity to both βarr1_E92 and βarr1_P120 in the SH3–βarr1–V2Rpp–Fab complex. As E92 and P120 are more than 20 Å apart, we hypothesized that the SH3 domain might independently bind at two sites of βarr1. Interestingly, complex formation for βarr1_P120 was more efficient in the presence of V2Rpp and Fab30, whereas βarr1_E92 forms the complex equally well regardless of activation (Fig. 1E). A few other residues in SH3 (e.g., N135C, Y92C, E115C) and βarr1 (P88C, P91C) formed the cross-linked complex to a lesser degree. Complex formation via these multiple residues suggests the dynamic nature of the SH3–βarr1 interfaces (Fig. 1C). To evaluate whether βarr1 can bind SH3 at two distinct sites, we used isothermal titration calorimetry (ITC) to estimate the affinity and the stoichiometry of SH3 binding to βarr1–V2Rpp (Fig. 1F). The integrated heat curve revealed two binding events: one with Kd of ~6 μM and the other with a significantly lower affinity of ~50 μM. The favorable entropy (-TΔS) suggests that in both sites, SH3–hydrophobic

interactions drive βarr1 binding. Furthermore, the favorable enthalpy (ΔH) at the higher affinity site indicates some contribution from hydrogen bonding and van der Waals forces.

βarr1 binds to the aromatic surface of SH3 and activates Src by SH3 domain displacement

To elucidate the molecular mechanism of SH3 recruitment by βarr1, we formed the cross-linked complexes with the best mutant pairs in each site: SH3_95C–βarr1_120C and SH3_95C–βarr1_92C and determined the structures by cryo-EM (Fig. 2, fig. S1-S2, table S1). The map obtained from the SH3_95C–βarr1_120C complex has a global resolution of 3.5 Å and showed a rigid interaction with SH3 in the central crest area of βarr1 (hereafter referred to as SH3–βarr1-CC) (Fig. 2A, fig. S2A). The complex was activated by V2Rpp and stabilized by Fab30 and nanobody 32 (Nb32) (*29*). In the SH3–βarr1-CC complex, βarr1 adopts an active conformation (*30*), characterized by C-tail displacement and inter-domain rotation, and binds to the hydrophobic surface of SH3 containing residues from the RT loop, nSrc loop and the 3_{10} helix (Fig. 2). In the SH3–βarr1-CC complex, βarr1 interacts with SH3 using β-strand V (residues 75-80) in the N domain and a part of the lariat loop in the C domain (Fig. 2B, Movie S1). Y90 and Y136 in SH3 interact with F75 in βarr1. W118 in SH3 makes a hydrogen bond with the main chain oxygen of D78 (Fig. 2B). The side chains of Y136 and N135 in SH3 are well-placed to make hydrogen bonds with the main chain oxygen of R76 in βarr1. Additional hydrogen bond appears to be formed by the main chain oxygen of E93 in SH3 and the side chain of N122 in βarr1.

The SH3_95C–βarr1_92C complex was formed with V2Rpp and Fab30 but without Nb32, as Nb32 appeared to prevent complex formation, most likely due to the steric clashes with SH3. Whereas the SH3–βarr1-CC complex has a clearly resolved density for SH3, in the SH3–βarr1-N complex the density for SH3 is weaker (local resolution is 4.2-4.6 Å) since SH3 binds to a flexible loop of βarr1, ^{87}FPPAPEDK^{94} motif (Fig. 2C, fig S2B). To place the SH3 domain, we used molecular dynamics flexible fitting (MDFF) constrained by the position of the disulfide bond (βarr1_92 and SH3_95). Similar to the SH3–βarr1-CC complex, βarr1 binds the aromatic surface of SH3. The polyproline region of βarr1 (P88-P91) appears to interact with W118, Y136, Y92, and P133 in SH3 (Fig. 2D, Movie S2). To verify the interaction interface between βarr1 and SH3, we introduced mutations in SH3 and βarr1 and tested the binding by pull-down assay (Fig. 2E, 2F). SH3 mutants Y90A_Y136A and Y92C_W118A_Y136A showed a drastically reduced ability to bind βarr1 (Fig. 2E). Similarly, less SH3 was bound by proline-deficient βarr1 mutants, suggesting the critical role of these residues for SH3–βarr1 interactions (Fig. 2F).

We then compared the mechanisms of SH3 recruitment by βarr1 with other SH3-binding proteins: Nef, ELMO1, ubiquitin, and ubiquitin-like domain of parkin (*17-21*). In all structures, SH3 uses the same hydrophobic surface to bind its partner protein (fig. S3). The βarr1-N site is similar to the canonical polyproline-rich motif on Nef and ELMO1, except that the polyproline sequence in βarr1 is shorter (fig. S3A, S3C). In contrast, the βarr1-CC site of βarr1 exhibits a drastically different binding mode by using phenylalanine and several charged and polar residues to recruit SH3 (Fig. 2B, S3D, S3E). Intriguingly, non-canonical specificities were previously observed for many SH3 domains (*15, 31*). For example, the SH3 domain of Sla1 endocytic protein interacts with histidine and hydrophobic residues of ubiquitin (fig. S3E) (*19*). However, this is the first time that different recognition mechanisms have been shown for the same SH3 domain in a single protein.

To understand how βarr1 activates Src, we aimed to determine the structure of βarr1 in complex with three-domain Src (SH3-SH2-SH1, residues 83-533). First, we tested by disulfide trapping whether Src_R95C binds to two sites of βarr1. As expected, we observed the formation of Src–βarr1 complexes in two polyproline regions of βarr1 by βarr1_120C and βarr1_92C, consistent with the data obtained for the isolated SH3 domain (fig. S4A). As βarr1_120C formed the highest

amount of the cross-linked complex (fig. S4A-S4B), we used it to form the complex with Src_R95C and determined its structure by cryo-EM (Fig. 3, fig. S4C, fig. S5A-S5C, table S1). Similarly to the SH3–βarr1-CC complex, βarr1 was activated by V2Rpp and stabilized by Fab30 and Nb32. The 2D classes of the complex show fuzzy density around the SH3 domain suggesting that the SH2 and SH1 domains of Src are very flexible (Fig. 3A). The final cryoEM map has a resolution of 3.3 Å with a clear density for the SH3 domain (Fig. 3B, fig. S5A-S5C). The superposition of SH3–βarr1-CC and the Src–βarr1 revealed a translational shift of 2.0-2.2 Å of the SH3 domain towards the central crest of βarr1 in the Src–βarr1 complex (fig. S5D). The orientation of SH3 in Src–βarr1 and the interaction network with βarr1 are similar to the SH3–βarr1-CC complex (fig. S5D). The SH2 and SH1 domains were not resolved in the final map suggesting they are too flexible (Fig. 3B). Filtering the map to a lower resolution (15 Å) revealed the density attributable to SH2 but not to SH1 (Fig. 3D). These observations support that SH1 and SH2 are flexible and that SH3 in Src–βarr1 does not interact with the autoinhibitory SH2-SH1 linker.

Src activity is tightly regulated by three mechanisms of intramolecular interactions named the latch, clamp, and switch that conformationally restrict SH1, the catalytic domain of Src (*32, 33*) (Fig. 3E, fig. S6). The latch involves phosphorylation of regulatory tyrosine Y527 and its binding to SH2; the clamp mediates binding of SH3 and SH2 to SH1 and additionally binding of SH3 to the SH2-SH1 linker; the switch involves the conformational change of the Src activation loop in SH1 (Fig. 3E). Unlatching, unclamping, and switching are required for full activation of Src. In the inactive Src structure, the RT loop, the 3_{10} helix and the nSrc loop of the SH3 domain bind to the SH2-SH1 linker and the small lobe of the SH1 domain thus engaging the clamp (fig. S6A) (*33*). The long SH2-SH1 linker (residues 230-264) has only one proline to bind SH3, and it can be displaced by a more potent polyproline motif (*34, 35*). Both βarr1-N and βarr1-CC interact with the RT loop and the 3_{10} helix of SH3 (Fig. 2B, 2D, Fig. 3C, fig. S6B, S6C), suggesting that βarr1 binding releases the SH2-SH1 linker and the SH1 domain. Indeed, densities for the SH1-SH2 linker or SH1 were not observed in the Src–βarr1 structure (Fig. 3). The long (35 residues) and flexible SH1-SH2 linker not bound to SH3 allows the unrestricted movement of SH1. Fully released SH1 unconstrained by interactions with other domains is accessible for trans-autophosphorylation and full activation (Fig. 3E). Therefore, βarr1 binding to SH3 disrupts the clamp mechanism of Src autoinhibition and thus promotes Src activation (Movie S3).

SH3 binding induces conformational changes in βarr1

To validate the structural information, we tested the solvent accessibility of free βarr1 and V2Rpp-activated βarr1 in the presence of SH3 by hydrogen–deuterium exchange mass spectrometry (HDX-MS) (Fig. 4A). Both free βarr1 and V2Rpp-activated βarr1 showed a considerable decrease in HDX rate in both the βarr1-CC and the βarr1-N sites upon SH3 binding (Fig. 4A, 4B).

Interestingly, SH3 binding to βarr1 induces significant conformational changes in βarr1 observed in the structural data and corroborated by the HDX experiments (Fig. 4A). The most dramatic changes are observed in the central crest region of βarr1 in the SH3–βarr1-CC and Src–βarr1 complexes. SH3 binding to βarr1-CC drastically changes the position of β-strand V: it shows a downward and the inward movement by ~9 Å and displays a two-residue offset in its N-terminal part and a three-residue offset in its C-terminal part as compared to the active structure of βarr1 without SH3 (Fig. 4C). Furthermore, the finger loop is contracted and resembles the conformation in inactive βarr1 (Fig. 4C). Similarly, the middle loop in SH3–βarr1-CC adopts an intermediate conformation between the fully active and fully inactive βarr1 crystal structures (Fig. 4C). While we cannot rule out that these differences may come from crystal packing constraints or the allosteric effects from binding to GPCRs (*11-14*), it is tempting to speculate that the changes

observed in the central crest region upon binding to Src might affect the coupling of βarr1 to the receptor.

Interestingly, region 149-166 showed a significant decrease in HDX (Fig. 4A), possibly due to its proximity to the SH3 domain in the βarr1-CC site. This is consistent with this loop becoming less dynamic when SH3 binds to βarr1 while not undergoing a major structural rearrangement (fig. S7A). Importantly, no changes in HDX were observed in the C-tail of βarr1 (fig. S7B) and its polar core (Fig. 4A), suggesting that SH3 binding does not cause βarr1 activation. We also tested the solvent accessibility of SH3 in the presence of free βarr1 and V2Rpp-activated βarr1 (fig. S7C, fig. S7D). In both cases we observed a decrease in the HDX uptake in the C-terminal part of the RT loop, nSrc loop, and the 3_{10} helix (fig. S7D), consistent with the structures and the pull-down data (Fig. 2E). A comparison of SH3 domains in the Src–βarr1 complex and the crystal structure of Src (PDB: 1FMK) revealed structural rearrangement in the 3_{10} helix and the nSrc loop of SH3. The interaction of βarr1 with the 3_{10} helix converts it into a loop in the Src–βarr1 complex (fig. S7E).

Barr1-N and βarr1-CC sites have different functionalities

We next sought to elucidate the physiological consequences of SH3 binding to βarr1-N and βarr1-CC. As shown previously, the βarr1–V2Rpp–Fab complex allosterically activates wild-type Src, and the activation is dependent on βarr1 binding to the SH3 domain of the kinase (*8*). Therefore, we generated a series of βarr1 mutants in βarr1-N and βarr1-CC sites and measured the βarr1-mediated activation of Src *in vitro*. Whereas V2Rpp-activated βarr1 WT increases Src activity in the *in vitro* kinase assay, all proline-deficient βarr1 mutants failed to activate Src (Fig. 5A, fig. S8A). These results are consistent with the pull-down data (Fig. 2F), where all proline-deficient βarr1 mutants showed reduced SH3 binding. Similarly, βarr1 mutants showed a significant decrease in Src activation in HEK-293 βarr1/βarr2 dKO (CRISPR-Cas9-based βarr1/βarr2 double knock-out) cells (*36*) after stimulation of chimeric β2-adrenergic receptor carrying vasopressin 2 receptor tail (β2V2R) with BI-167107 (Fig. 5B). We then tested the effect of the βarr1 mutations on activation of endogenous Src in HEK-293 βarr1/βarr2 dKO cells downstream of dopamine 1 (D1R) receptor (Fig. 5C). While basal levels of phospho-Src were detected in all non-stimulated cells, addition of dopamine led to a significant increase in phospho-Src in βarr1 WT transfected cells. In contrast, none of the βarr1 mutants showed a response to dopamine stimulation, suggesting their reduced ability to activate Src (Fig. 5C). Therefore, both βarr1-CC and βarr1-N sites mediate Src activation *in vitro* and in cells downstream of two receptors, β2V2R and D1R.

We reasoned that binding of the SH3 domain of Src to the central crest region of βarr1 (βarr1-CC) might hinder the engagement of βarr1 with the transmembrane bundle of GPCRs. For example, the structural superpositions of Src–βarr1 with the structure of formoterol-bound chimeric β1-adrenergic receptor carrying vasopressin 2 receptor tail (β1V2R) (PDB: 6TKO) (*13*) indicate the possible steric clashes of the helical bundle of GPCRs with βarr1-bound SH3 (Fig. 5D). Furthermore, βarr1 finger loop mediating core coupling to the receptor is contracted in the SH3–βarr1-CC complex, as opposed to the extended conformation in GPCR–βarr1 structures (Fig. 4C) (*11-14*). We, therefore, evaluated whether excess of SH3 would interfere with the core coupling of βarr1 to the phosphorylated V2R in membranes. We labeled the finger loop of βarr1 V70C with an environment sensitive bimane fluorophore (mBr) and measured the changes in fluorescence emission spectra with and without SH3. Upon stimulation of the phosphorylated V2R with the agonist - arginine-vasopressin peptide (AVP), the finger loop of βarr1 V70C-mBr binds to the receptor core, leading to a ~50% increase in bimane fluorescence (Fig. 5E). The presence of SH3 significantly reduces this effect, suggesting that SH3 binding to βarr1 sterically hinders the core coupling of βarr1 to V2R (Fig. 5E). Similar results were obtained with the purified phosphorylated

chimeric M2-muscarinic receptor reconstituted in MSP1D1E3 nanodiscs (fig. S8B). Therefore, it appears that Src binding to βarr1 can directly affect the conformational equilibrium of GPCR–βarr1 complexes by disrupting the fully engaged "core" conformation.

Discussion

GPCRs convert extracellular signals into cellular responses via two major transducers, the G proteins and βarrs, which in turn interact with their downstream effectors. The rapid development of cryo-EM has greatly advanced our understanding of how GPCRs recruit signal transducers. In contrast, little is known about how the transducers allosterically regulate effector enzymes. Currently, there is one structure of an activated G protein αs subunit bound to adenylyl cyclase AC9 (*37*), and no structures of effector signaling complexes. Capturing dynamic transient complexes has long represented a significant challenge in structural biology, necessitating high levels of engineering to obtain structural information that would otherwise be intractable. Disulfide cross-linking has been widely used in the field, including to obtain the structures of GPCR-chemokine complexes (*38*) and the first active GPCR-ligand structure (*39*). Disulfide trapping has the caveat of locally restraining the interaction, but it is less prone to non-specific artefacts than chemical cross-linking and is less likely to affect protein folding or expression as compared to the genetic fusion approach. Using disulfide cross-linking we determined the first high-resolution structures of a βarr-effector signaling hub, βarr1 in complex with tyrosine kinase Src. We demonstrated that SH3 binds to two distinct sites of βarr1, one in the distal part of the N-domain (βarr1-N) and the other in the central crest region (βarr1-CC). Our study corroborates earlier findings that Src–βarr1 interaction is dependent on proline residues P88-P91 and P120-121, and elucidates the structural basis of Src recruitment and activation by βarr1 (*4, 7, 8*). Unexpectedly, residues P120-121 are not directly engaged in the interaction with SH3, but their mutation may disrupt the interface indirectly. Elucidating their role in this interaction will require further studies. Furthermore, disulfide trapping used to stabilize the transient SH3–βarr1 complexes constrains the binding interface and captures only one state of the dynamic complex.

Src-binding proteins activate Src family kinases by binding the SH3 domain (*34, 40*), SH2 domain (*41, 42*), or both domains (*43*) and thereby disrupt the intramolecular interactions inhibiting the kinase activity (*44, 45*). Earlier studies showed that βarr1 mediates allosteric activation of Src through the SH3 domain (*7, 8*). Using site-specific fluorescence labeling of Src, Yang *et al.* showed disruption of SH3/SH1 and SH3/SH2 interactions in the presence of GPCR–βarr1 complex (*7*). Our structures of SH3–βarr1 and Src–βarr1 complexes elucidate the precise molecular mechanism of βarr1-mediated allosteric activation of Src (Fig. 3, Movie S3). The residues of the RT loop, the 3_{10} helix and the nSrc loop of SH3 involved in maintaining the autoinhibitory conformation of Src engage with βarr1 instead of the SH2-SH1 linker that maintains the autoinhibitory conformation of Src, thus releasing the SH1 domain. To corroborate this, we observe in the Src–βarr1 complex that SH3 binds to βarr1, whereas the SH2 and SH1 domains are not resolved suggesting their unrestricted movement as in the active open conformation of Src. Even though we have determined the structure of Src bound to one SH3-binding site in βarr1 (βarr1-CC site), structural superpositions (fig. S6B) as well as mutagenesis experiments (Fig. 5) suggest a similar activation mechanism as in the βarr1-N site.

βarr1 is also known to interact with the SH1 domain of Src (*8, 46*). While we do not observe such interaction in the current data, additional functional and structural studies of the GPCR–βarr–Src signaling axis will be required to confirm and understand the physiological role of this interaction. In addition to the conformational activation of the kinase, βarrs might also facilitate Src trans-autophosphorylation by bringing two Src molecules into close proximity. Furthermore, βarrs might also bring Src in contact with its potential substrates, as seen in focal adhesion kinase (FAK)–Src

signaling complexes (*47*). Interestingly, binding of SH3 or Src to βarr1-CC site introduces structural rearrangements in βarr1, especially in the central crest region, that may influence βarr1 interactions with receptors and other signaling components (Fig. 4C). We demonstrate that binding of SH3 interferes with βarr1 coupling to the receptor core (Fig. 5E, fig. S8B), thus potentially affecting receptor desensitization and termination of G-protein-mediated signaling. Reduction of core coupling upon SH3 binding suggests that the "tail" conformation of GPCR–βarr1 complexes might be more favorable for Src activation. However, βarr1 with deleted finger loop (βarr1 ΔFL) responsible for core interaction did not activate Src more efficiently than wild-type βarr1 (*8*). βarr1 activates Src via two sites for SH3. In the "core" conformation the activation can occur via the distant βarr1-N site, whereas in the "tail" conformation either site can be used (Fig. S8C). Still, βarr1 can only bind one molecule of Src at a time due to steric constraints. Therefore, we cannot claim that the "tail" conformation is preferred for Src activation. On the other hand, if Src is present at a high molar excess to βarr1, it will shift the conformational equilibrium of GPCR–βarr1 complexes towards the "tail" conformation (Fig. 5E, fig. S8B).

Barrs, originally discovered as proteins mediating GPCR desensitization (*48, 49*), are now commonly recognized as signal transducers (*3, 7, 8, 50*). However, there is still some controversy in the field as to whether βarrs are just modulators of G-protein-mediated signaling events (*51*) or rather bona fide signal transducers in their own right. Here we provide the first structural evidence to demonstrate that βarr1 indeed acts as an independent signal transducer by recruiting the SH3 domain of Src to confer allosteric activation of the kinase. Taken together, this work provides initial insights into the conformational mechanisms driving the first discovered βarr-mediated signaling pathways. Thus, these findings represent an important step forward towards understanding how allosteric regulation of GPCR signaling is achieved at the effector level.

Acknowledgments: We thank Nilakshee Bhattacharya at the Duke University Shared Materials Instrumentation Facility (SMIF) and Joshua Strauss at the cryo-EM core at the University of North Carolina Chapel Hill for assistance with microscope operation. We thank Seung Ahn and Liyin Huang for helpful discussions throughout this work. We are grateful to Yangyang Li for administrative assistance.

Funding:

National Institutes of Health grant R01 HL16037 (RJL)

National Institutes of Health grant R35GM133598 (AdG)

Human Frontier Science Program, postdoctoral fellowship LT000174/2018 (NP)

European Molecular Biology Organization, postdoctoral fellowship ALTF 1071-2017 (NP)

RJL is an Investigator of the Howard Hughes Medical Institute

Author contributions:

Conceptualization: NP, AdG, RJL

Methodology: NP, BNT, BP, LL, HB, DKB, XZ

Investigation: NP, BNT, LL, HB, RRA, JK, AWK, BP, DKB, SL, XZ

Visualization: NP, BNT, LL, RRA, SL, AWK, BP

Funding acquisition: AdG, RJL

Project administration: AdG, RJL

Supervision: AdG, RJL

Writing – original draft: NP, RJL

Writing – review & editing: NP, BNT, HB, AWK, BP, AdG, RJL

Competing interests: The authors declare that they have no conflicts of interest with the contents of this article.

Data and materials availability: The coordinates and the corresponding cryo-EM maps were deposited at the Protein Data Bank and the EMDB with the accession codes 9CX3 and EMD-45977 (SH3–βarr1-CC complex), 9CX9 and EMD-45982 (SH3–βarr1-N complex), 9BT8 and EMD-44881 (Src–βarr1 complex), respectively. All data are available in the main text or the supplementary materials. The materials presented are available upon request from Robert J. Lefkowitz (lefko001@receptor-biol.duke.edu).

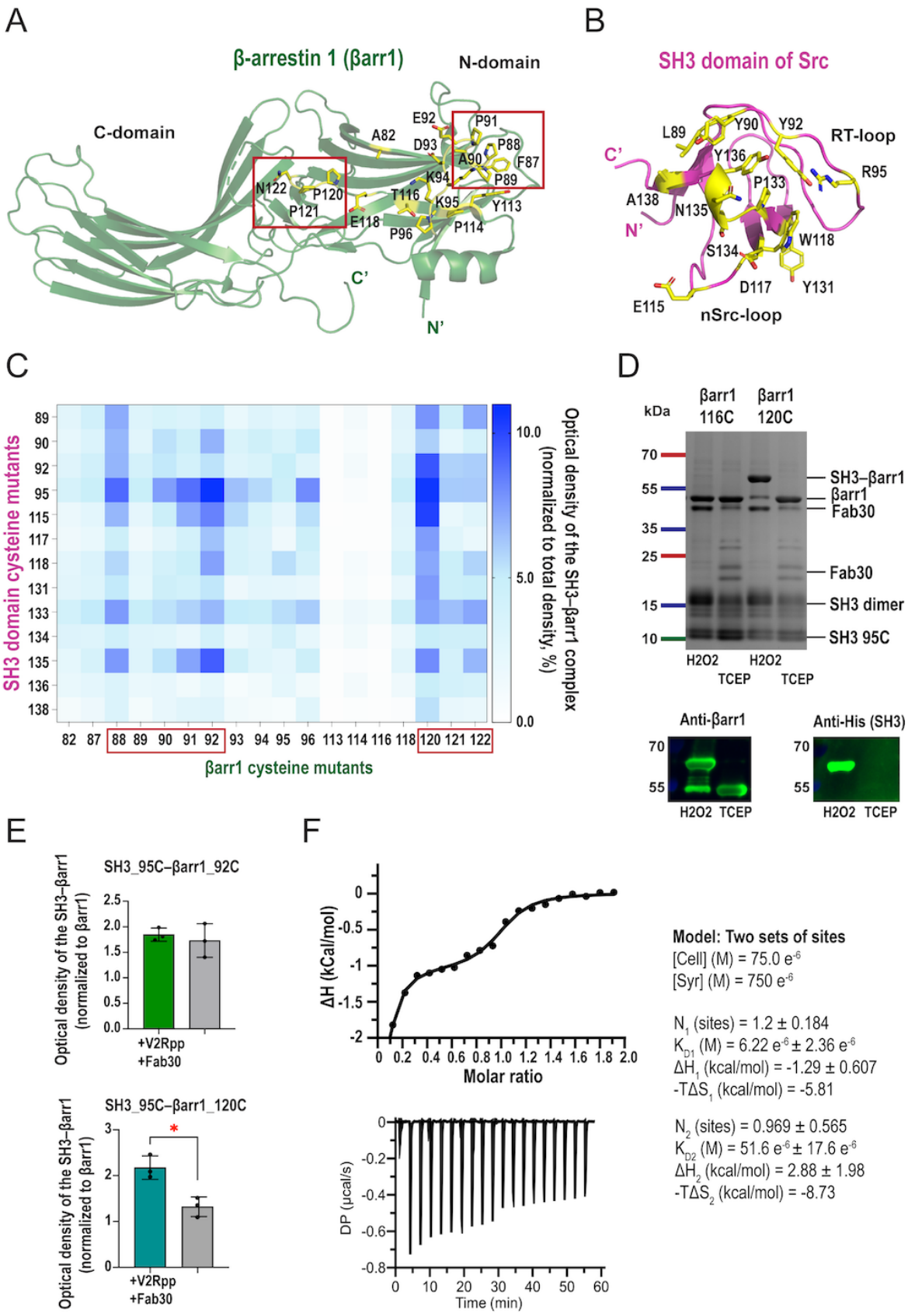

Figure 1. Disulfide trapping reveals formation of SH3–βarr1 complexes in two regions of βarr1. (**A, B**) Structures of βarr1 (green, PDB: 4JQI) and SH3 (magenta, PDB: 2PTK), cartoon representation. Residues used for disulfide trapping experiments are shown as sticks, colored in yellow and labeled. Proline regions of βarr1 are framed in red rectangles; RT and nSrc loops of SH3 are labeled. (**C**) Heatmap of different SH3–βarr1 cysteine-pair complexes revealed by disulfide trapping; densitometry analysis of Coomassie blue gels. The SH3–βarr1 complex band was normalized to the total density of all bands in each sample; the mean of at least three independent experiments is shown. Prior to disulfide trapping reactions, βarr1 was activated by a synthetic phosphopeptide mimicking the C-tail of vasopressin 2 receptor (V2Rpp) and stabilizing antibody Fab30. (**D**) Top: representative results of disulfide trapping, Coomassie blue gel. A 60-kDa band corresponding to the covalent SH3–βarr1 complex appears in reaction with βarr1_120C and SH3_R95C but not with βarr1_116C and SH3_R95C. Note that more than 80% βarr1_120C reacts with SH3 to form the complex. Bottom: Western blot of disulfide trapping reaction with βarr1_120C and SH3_R95C. 60-kDa band is detected by both βarr1 (A1CT) and anti-His (SH3) antibodies confirming that the band is the covalent SH3–βarr1 complex. (**E**) Densitometry analysis of SH3–βarr1 disulfide trapping with and without V2Rpp and Fab30. Individual data, mean ± standard deviation (SD) of three independent experiments is shown. Statistical analysis was performed using Student's t-test (*$p < 0.05$). (**F**) Isothermal titration calorimetry of SH3 binding to βarr1–V2Rpp. Left panel: integrated heat (after deducting heat of dilution) per injection of SH3 into βarr1–V2Rpp solution in the cell based on the molar ratio of each injection. Middle panel: raw titration data showing the heat rate associated with each dilution per injection versus time into βarr1–V2Rpp solution in the cell. Right panel: thermodynamic parameters of SH3–βarr1–V2Rpp. The data are representative of three independent experiments.

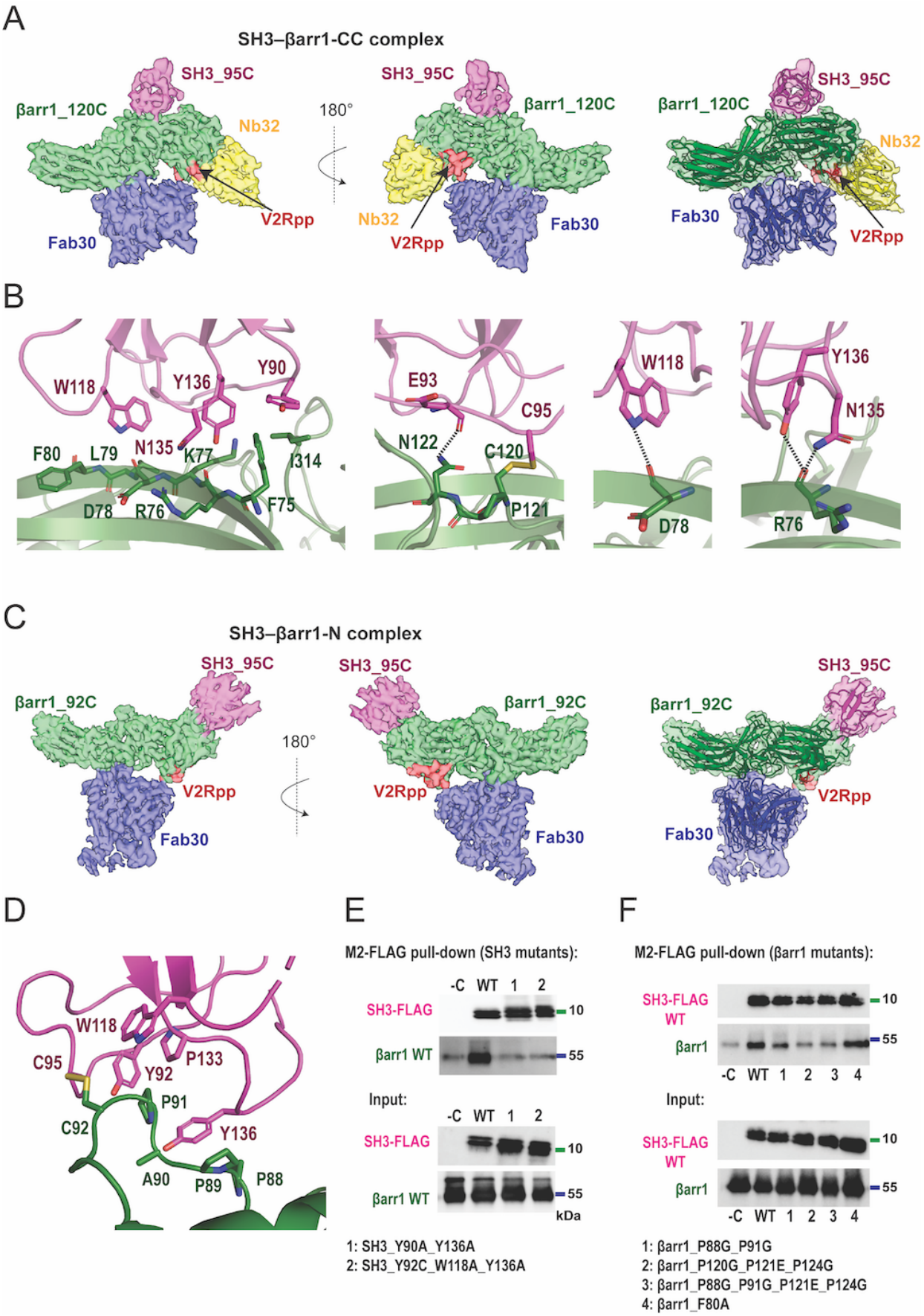

Figure 2. Cryo-EM structures of SH3–βarr1–V2Rpp–Fab complexes.
(**A**) Left and middle panels: Cryo-EM density map of the SH3–βarr1-CC complex in two orientations colored by subunit (green, βarr1; magenta, SH3; red, V2Rpp; blue, Fab30; yellow, Nb32). Right panel: Cryo-EM density map with fitted model of the SH3–βarr1-CC complex. Map contour level is 0.45. (**B**) Left panel: The interaction interface of SH3–βarr1-CC complex (green, βarr1; magenta, SH3), cartoon representation. Middle and right panel: Residues forming the hydrogen bonds (shown as dashed lines). (**C**) Left and middle panels: Cryo-EM density map of the SH3–βarr1-N complex in two orientations colored by subunit (green, βarr1; magenta, SH3; red, V2Rpp; blue, Fab30). Right panel: Cryo-EM density map with fitted model of the SH3–βarr1-N complex. Map contour level is 0.40. (**D**) The interaction interface of SH3–βarr1-N complex (green, βarr1; magenta, SH3), cartoon representation. The residues are shown as sticks and labeled. (**E**) M2-FLAG pull-down assay of SH3-FLAG mutants and βarr1 WT, representative Western blot (n=3). (**F**) M2-FLAG pull-down assay of SH3-FLAG WT and βarr1 mutants, representative Western blot (n=3).

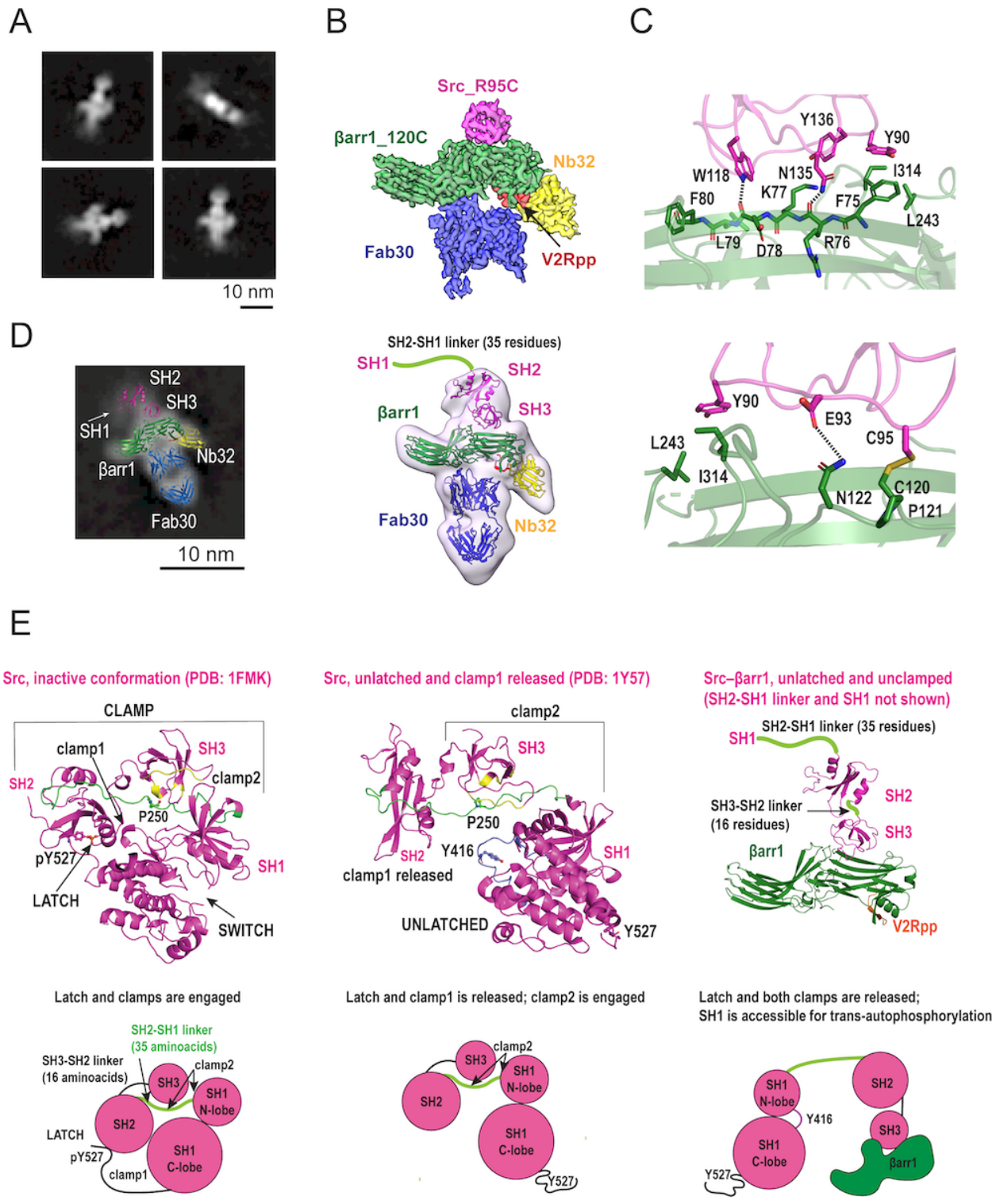

Figure 3. βarr1 binding to SH3 releases the catalytic domain of Src and promotes Src activation.

(A) Representative 2D classes of the Src–βarr1 complex. (**B**) Cryo-EM density map of the Src–βarr1 complex colored by subunit (green, βarr1; magenta, Src(SH3); red, V2Rpp; blue, Fab30; yellow, Nb32). Map contour level is 0.65. (**C**) The interaction interface of the Src–βarr1 complex (green, βarr1; magenta, Src (SH3 is shown), cartoon representation. The residues are shown as

sticks and labeled; the hydrogen bonds are shown as dashed lines. (**D**) Left panel: 2D class with the fitted model; right panel: cryo-EM density map of the Src–βarr1 complex low-pass filtered to 15 Å with the fitted model. Map contour level is 0.06. (**E**) Proposed mechanism of Src activation by βarr1. Left panel: structure of fully inhibited Src (PDB: 1FMK, left panel). Parts of SH3 interacting with βarr1 are colored in yellow. Middle panel: structure of partially inhibited Src (PDB: 1Y57, middle panel). Right panel: structure of the Src–βarr1 complex. The SH2 domain was fitted into the map low-pass filtered to 15 Å; the approximate position of SH1 is shown. SH2-SH1 linker is colored in green; residues critical for activation/autoinhibition are shown and labeled. βarr1 binding to SH3 releases the clamp mechanism of Src autoinhibition and drives Src activation.

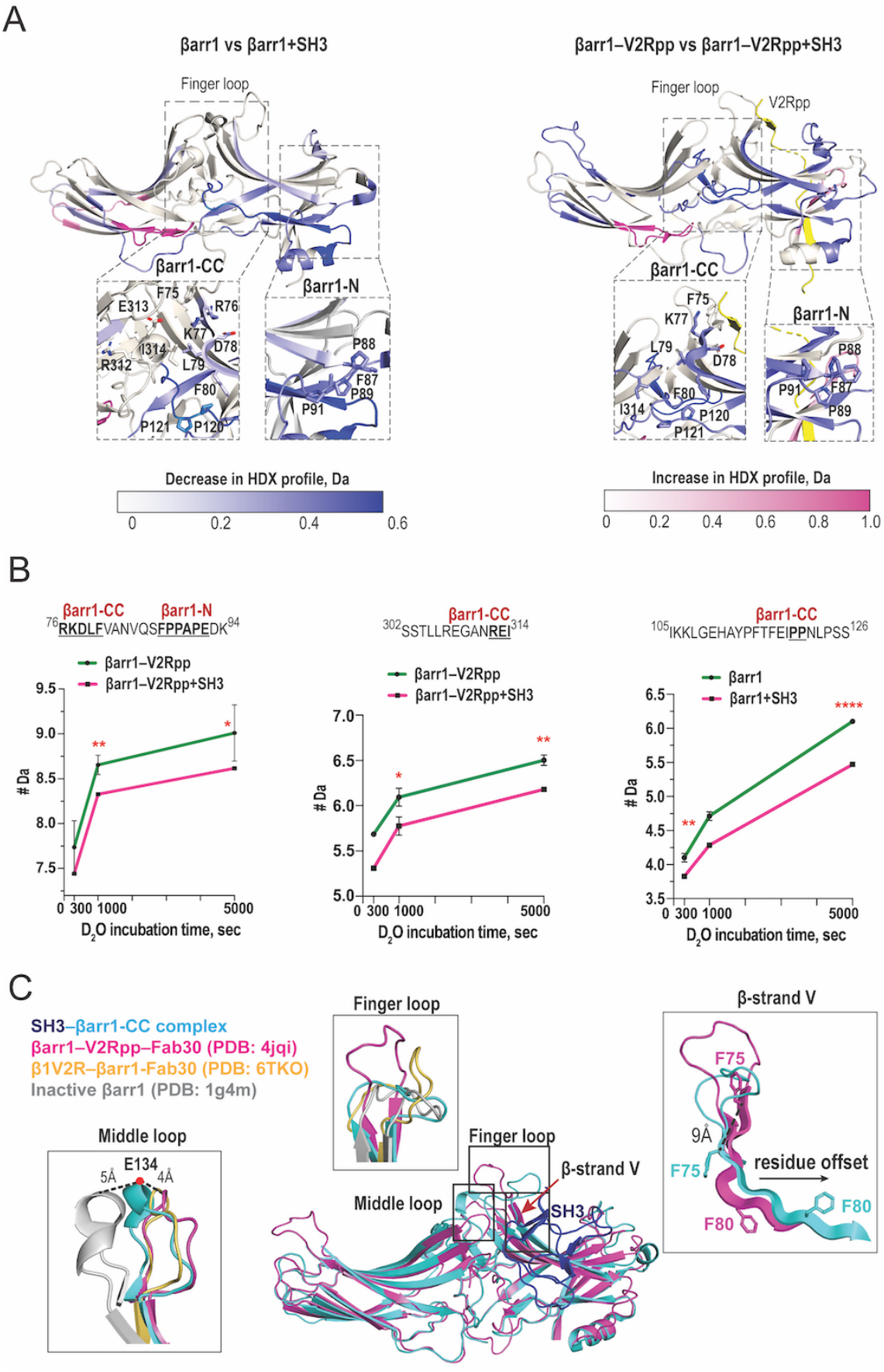

Figure 4. SH3 binding induces distinct conformational changes in βarr1

(A) The HDX profile changes in free βarr1 (PDB: 1G4M, grey) and V2Rpp-activated βarr1 (PDB: 4JQI, βarr1 - grey; V2Rpp - yellow) upon co-incubation with SH3. Regions with decreased and increased deuterium uptake are shaded in blue and red, respectively. Only regions that showed statistically significant differences between the states in deuterium uptake (>0.2 Da) in at least two peptides or at least two time points are indicated. Insets: focus on the βarr1-N and βarr1-CC sites; the residues are shown as sticks and labeled. (**B**) The HDX profile of corresponding peptides. Data represent the mean ± standard deviation (SD) of three independent experiments. Statistical analysis was performed using Student's t-test (**p < 0.01, ****p < 0.0001). (**C**) Conformational changes in βarr1 upon SH3 binding. Structures of βarr1 in SH3–βarr1-CC (cyan), βarr1–V2Rpp–Fab30 (PDB: 4JQI, magenta), the complex of chimeric β1AR with vasopressin 2 receptor tail (β1V2R) with βarr1–Fab30 (PDB: 6TKO, yellow) and inactive βarr1 (PDB: 1G4M, grey) are superimposed. Inset: focus on β-strand V, middle loop and finger loop. In the middle loop inset the distances between Cα atoms of E134 are indicated. In the β-strand V inset the distance between Cα atoms of F75 is shown.

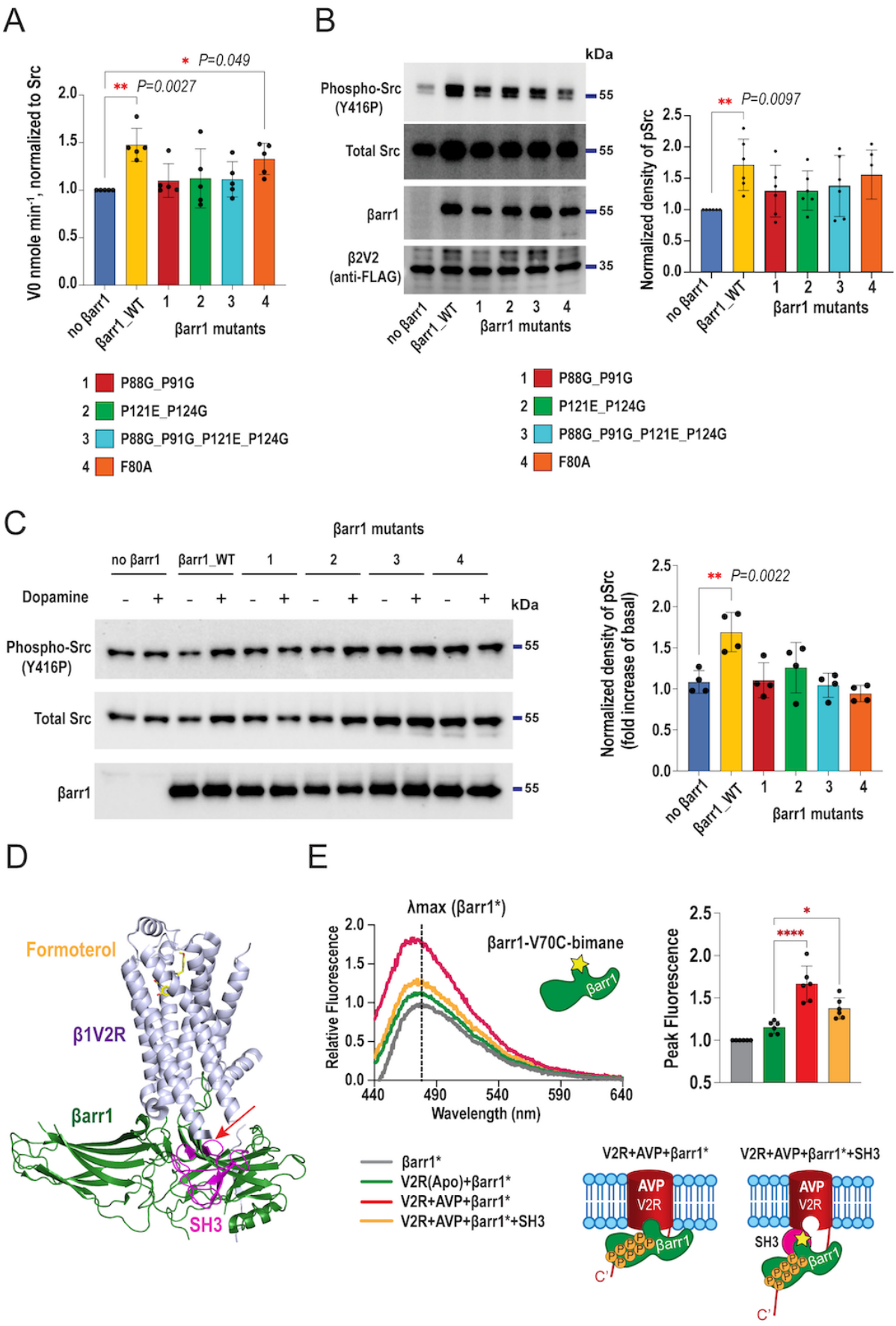

Figure 5. Physiological role of SH3-binding sites of βarr1

(**A**) Initial velocity of optimal Src peptide (AEEEIYGEFEAKKKK) phosphorylation by Src (V0) alone or in the presence of βarr1 WT or βarr1 mutants. V2Rpp was added to each reaction. Individual data, mean ±SD of five independent experiments is shown. Statistical differences were determined by one-way ANOVA and Dunnett's multiple comparison test. (**B**) Effect of βarr1 mutations in SH3 binding sites on Src activity downstream of β2V2. β2V2, Src and βarr1 were transiently expressed in HEK-293 βarr1/βarr2 dKO cells. 48 hours after transfection with 16-hour starvation, cells were stimulated with 10 uM of BI-167107 for 10 minutes at 37 °C and lysed. Left panel: representative Western blots. Right panel: densitometry analysis of Src phosphorylation normalized to Src phosphorylations in control cells (no βarr1 transfected). Statistical differences were determined by one-way ANOVA and Dunnett's multiple comparison test (n=6). (**C**) Effect of βarr1 mutations in SH3 binding sites on endogenous Src activity downstream of D1R. D1R and βarr1 were transiently expressed in HEK-293 βarr1/βarr2 dKO cells. 48 hours after transfection with 16-hour starvation, cells were stimulated with 10 uM of dopamine for 5 minutes at 37 °C and lysed. Left panel: representative Western blots. Right panel: densitometry analysis of Src phosphorylation normalized to phospho-Src in unstimulated cells. Statistical differences were determined by one-way ANOVA and Dunnett's multiple comparison test (n=4). βarr1 mutants numbering is the same as in (B). (**D**) Structural superposition of Src–βarr1 (SH3, magenta; βarr1, green) with the β1V2R–βarr1 complex (β1V2R, slate; PDB: 6TKO), cartoon representation. The clashing region is indicated with the red arrow. (**E**) SH3 binding interferes with the core coupling of βarr1 to phosphorylated V2R in membranes. Top left panel: representative experiment of βarr1 finger loop bimane fluorescence. Top right panel: peak fluorescence of βarr1 finger loop bimane; individual data, mean ±SD of six independent experiments is shown. Statistical differences were determined by one-way ANOVA and Dunnett's multiple comparison test (* - P=0.0174, **** - P<0.0001). Bottom panel: schematic of SH3-mediated disruption of βarr1 core coupling to V2R.

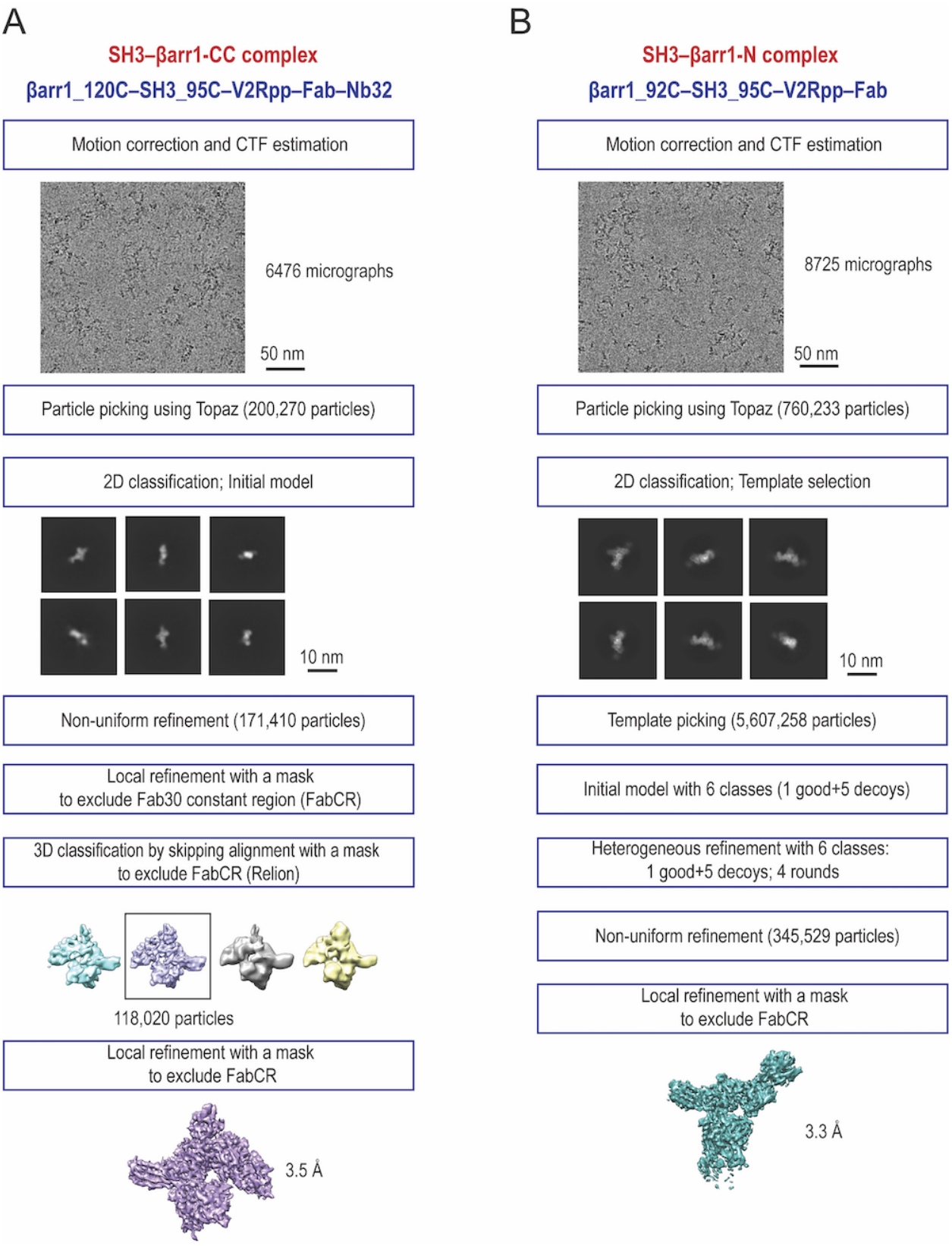

Figure S1. Flow chart of cryo-EM data processing of SH3–βarr1-CC (**A**) and SH3–βarr1-N (**B**) complexes.

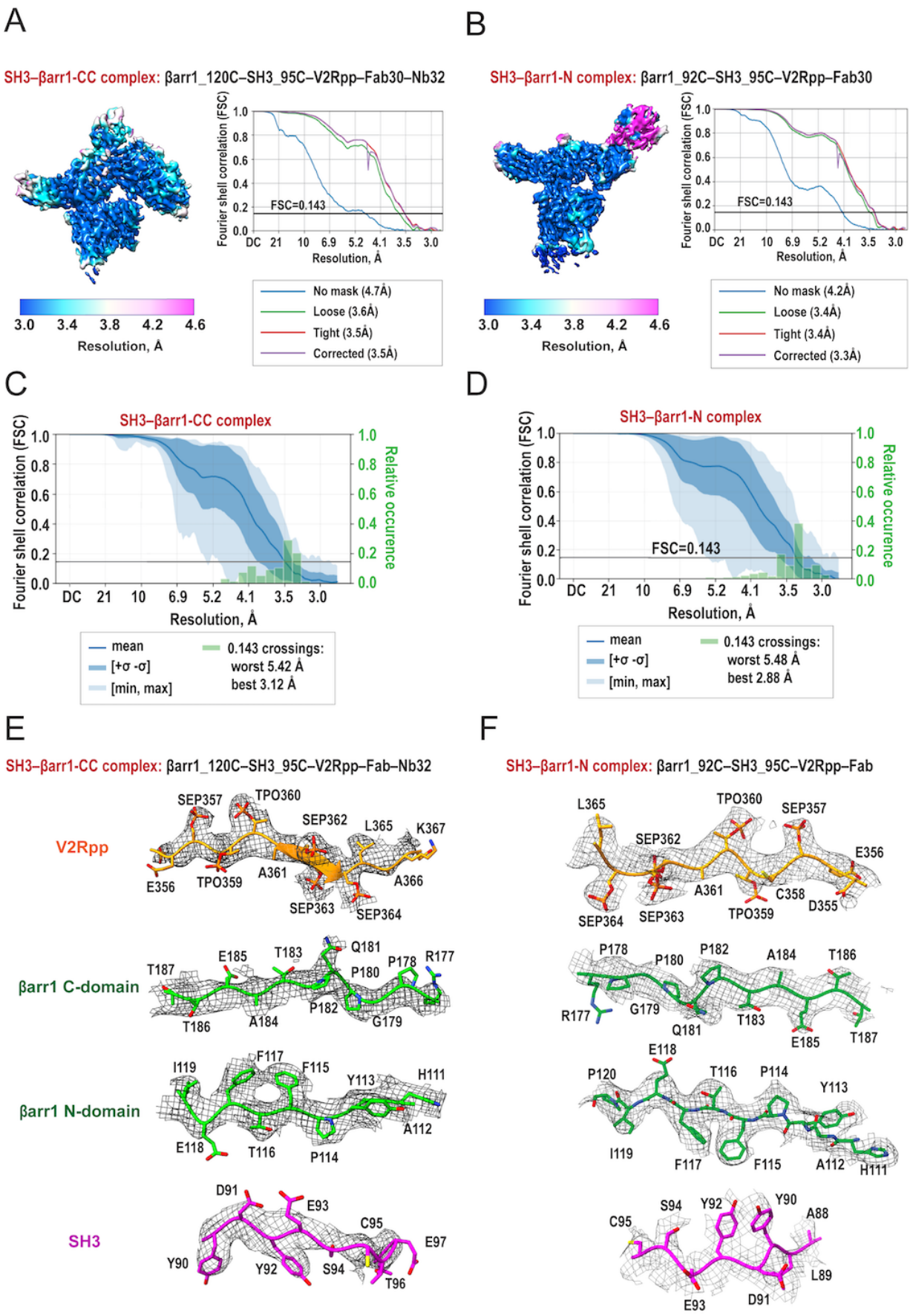

Figure S2. Cryo-electron microscopy of SH3–βarr1 complexes.

(**A, B**) Cryo-EM maps of SH3–βarr1-CC (A) and SH3–βarr1-N (B) coloured by local resolution and Fourier-shell correlation (FSC) curves of the final reconstructions; resolution is reported at the FSC threshold of 0.143. Map contour level is 0.45 for SH3–βarr1-CC and 0.38 for SH3–βarr1-N. (**C, D**) Summary of 3072 conical FSC of SH3–βarr1-CC (C) and SH3–βarr1-N (D), which indicate the presence of anisotropy in the maps. (**E, F**) Cryo-EM density at different parts of SH3–βarr1-CC (E) and SH3–βarr1-N (F). The upsample maps are used (0.69 Å/pix), map contour level is 0.13.

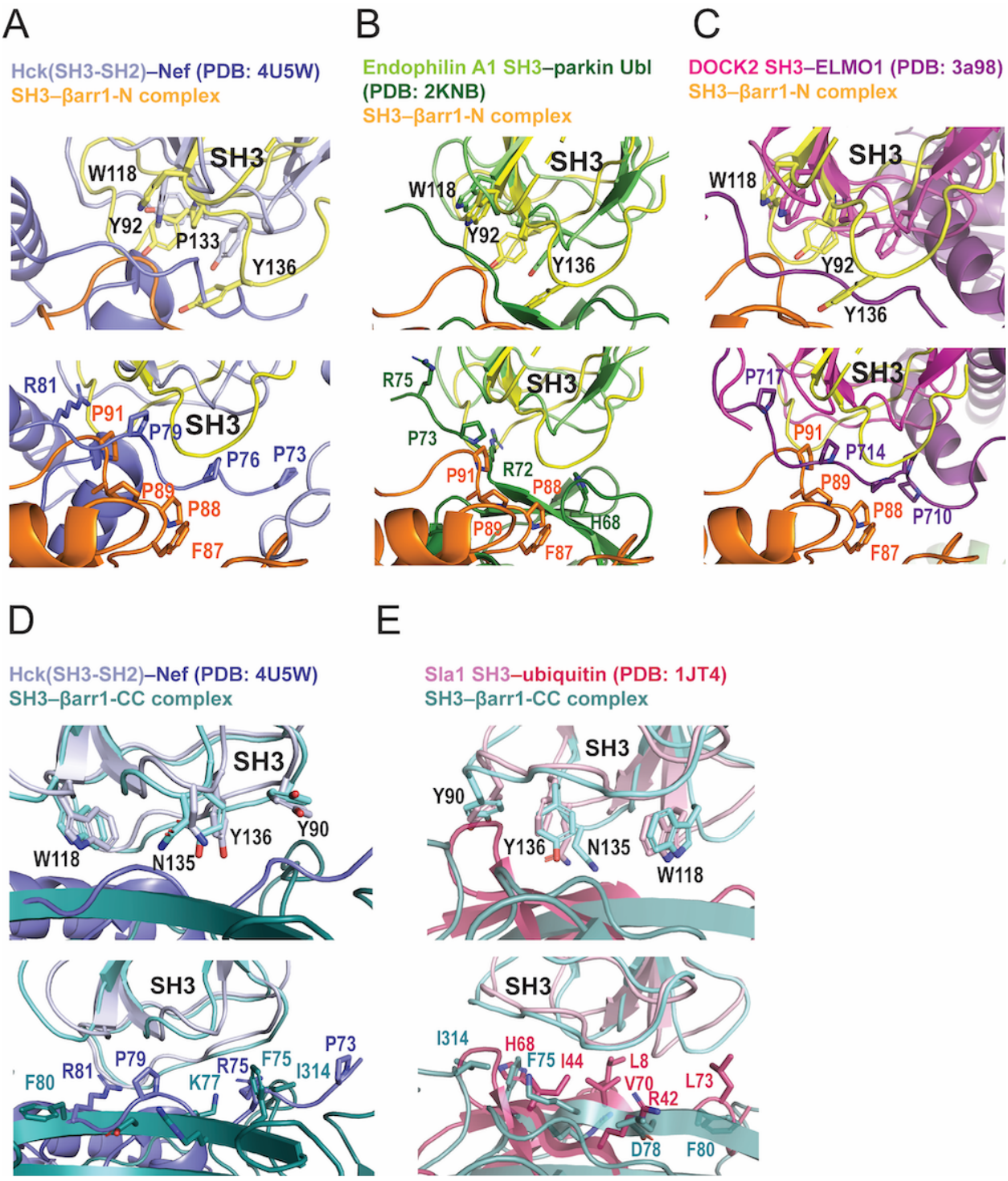

Figure S3. Structural superpositions of SH3 domains in SH3–βarr1-N (yellow), SH3–βarr1-CC (cyan) and other SH3-binding complexes

(**A, B, C**) Structural superpositions of SH3 domains in SH3–βarr1-N (yellow) and Hck(SH3-SH2)-Nef (slate) (A), endophilin A1 SH3–parkin Ubl (green) (B), DOCK2 SH3–ELMO 1 (magenta) (C), cartoon representation. Top panel shows the interacting residues in SH3 (Src SH3 numbering is used), the bottom panel shows interacting residues in βarr1 and the SH3-binding

protein. (**D, E**) Structural superpositions of SH3 domains in SH3–βarr1-CC (cyan) and Hck(SH3-SH2)-Nef (slate) (D), Sla1 SH3-ubiquitin (pink) (E), cartoon representation. Top panel shows the interacting residues in SH3, the bottom panel shows interacting residues in βarr1 and the SH3-binding protein.

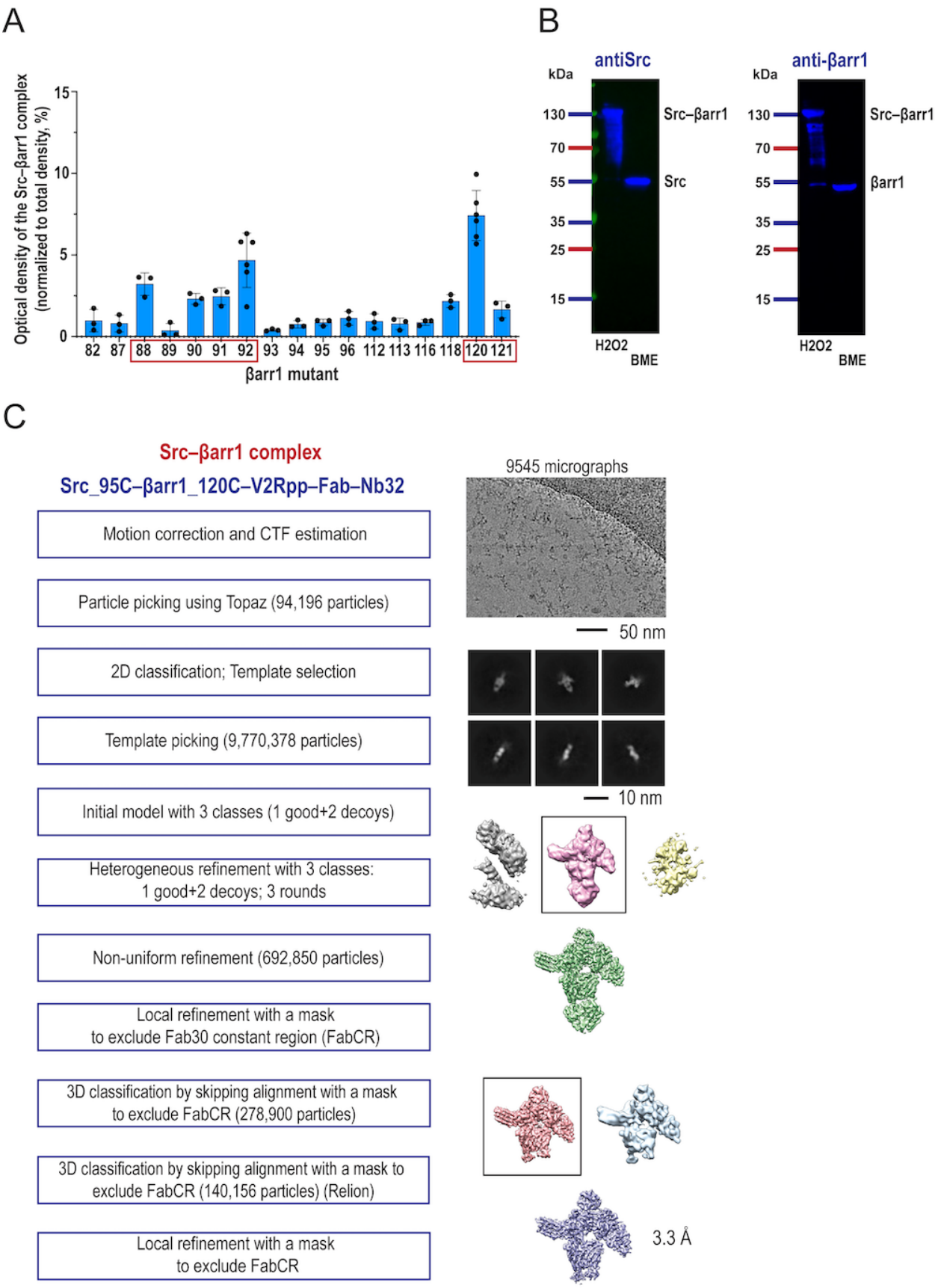

Figure S4. Complex formation and cryoEM data processing of Src–βarr1.

(**A**) Complex formation between Src_R95C and βarr1 mutants revealed by disulfide trapping; densitometry analysis of Coomassie blue gels. The Src–βarr1 complex band was normalized to the total density of all bands in each sample (individual data, mean ±SD, n=3-6). Prior to disulfide trapping reactions, βarr1 was activated by a synthetic phosphopeptide mimicking the C-tail of vasopressin 2 receptor (V2Rpp) and stabilizing antibody Fab30. (**B**) Western blot of disulfide trapping reaction with βarr1_120C and Src _R95C. 130-kDa band is detected by both βarr1 (A1CT) and anti-Src antibodies, confirming that the band is the covalent Src–βarr1 complex. **(C)** Flow chart of cryo-EM data processing of the Src–βarr1 complex.

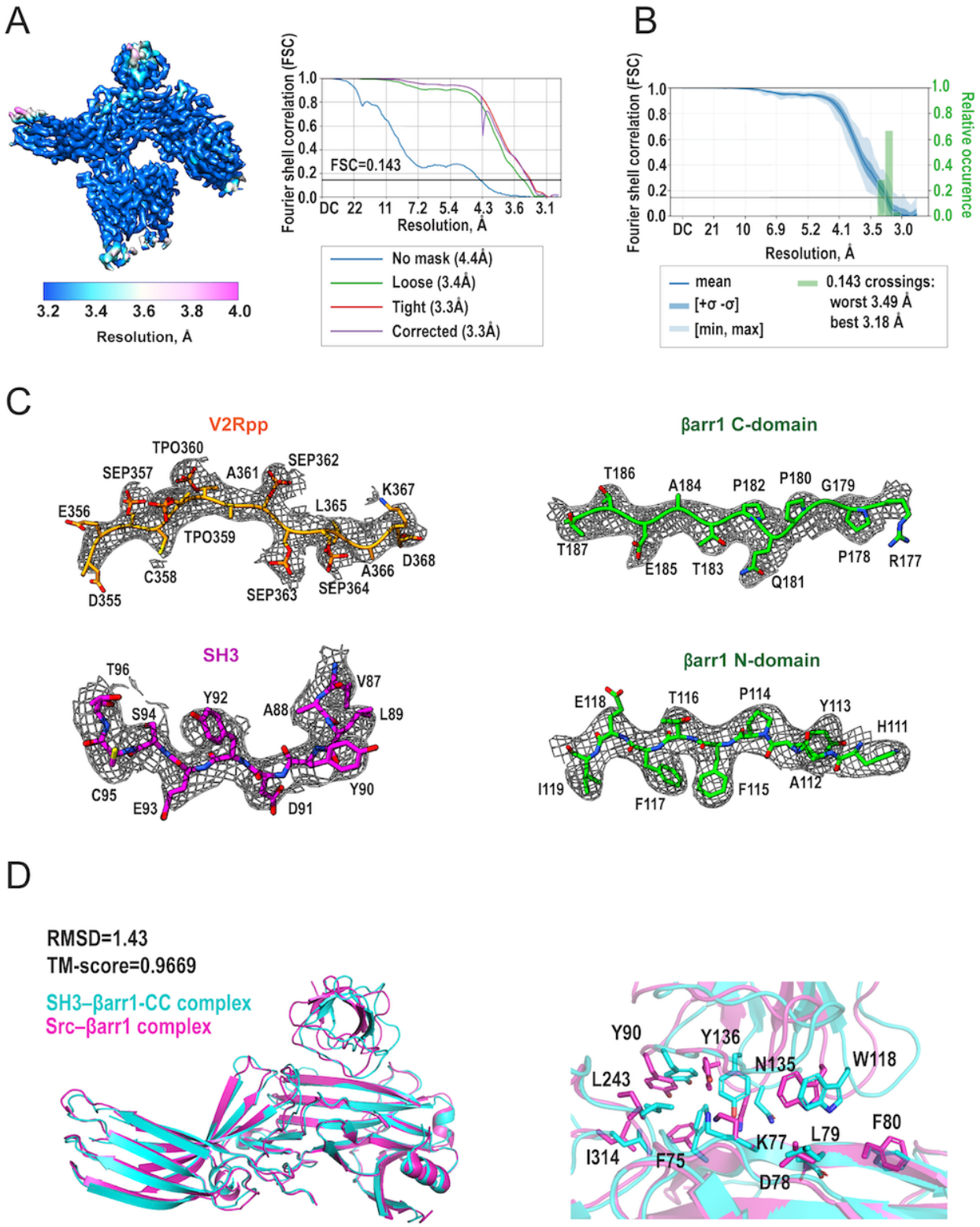

Figure S5. Cryo-electron microscopy of Src–βarr1.

(**A**) Cryo-EM map of the Src–βarr1 complex colored by local resolution (left panel) and Fourier-shell correlation (FSC) curves of the final reconstructions (right panel); resolution is reported at

the FSC threshold of 0.143. Map contour level is 0.55. (**B**) Summary of 3072 conical FSC of Src–βarr1 indicates no preferred orientation of the complex and no anisotropy of the map. (**C**) Cryo-EM density at different parts of Src–βarr1 map. The upsample maps are used (0.72 Å/pix), map contour level is 0.13. (**D**) The structural superposition of Src–βarr1 complex and SH3–βarr1-CC complex (Fab30, V2Rpp and Nb32 are not shown). RMSD and the TM-score of the structures was calculated using the TM-score function (*52*).

A

Src, inactive conformation (PDB: 1FMK)

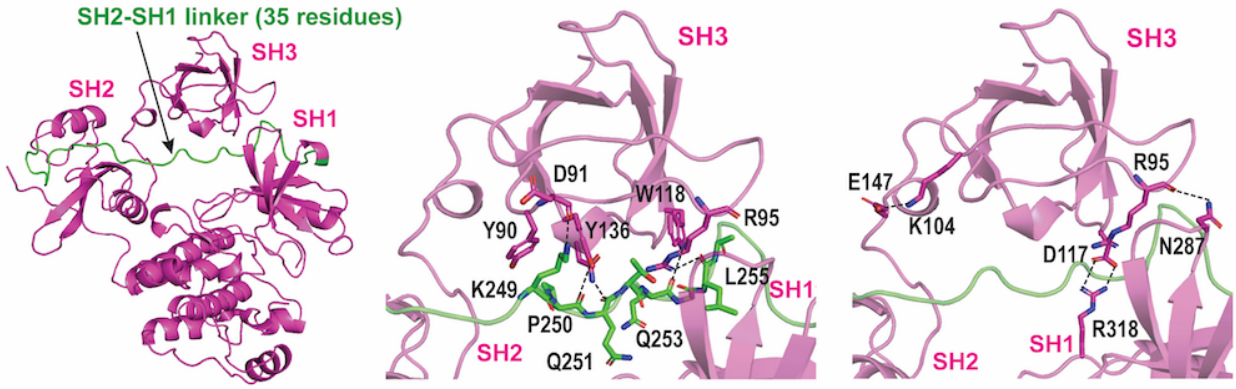

B

SH3–βarr1-N

Src, inactive conformation (PDB: 1FMK)

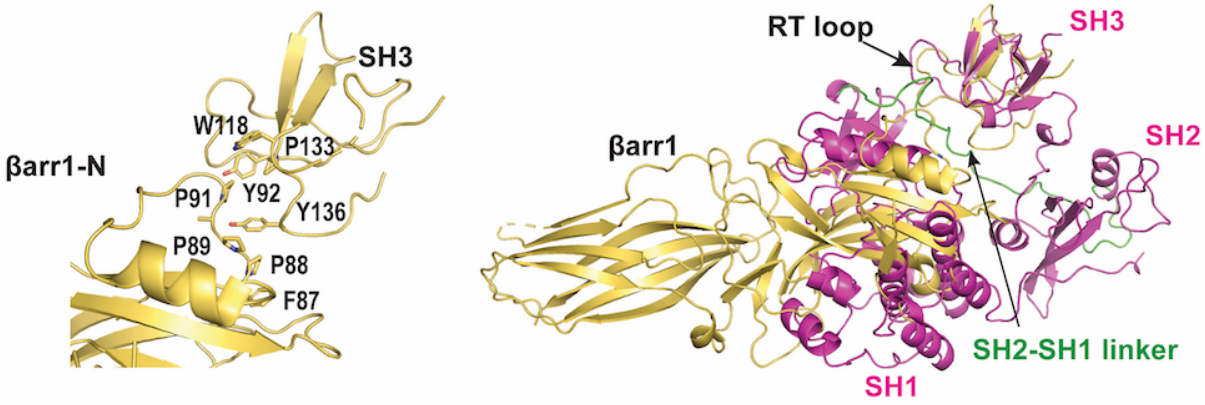

C

SH3–βarr1-CC

Src, inactive conformation (PDB: 1FMK)

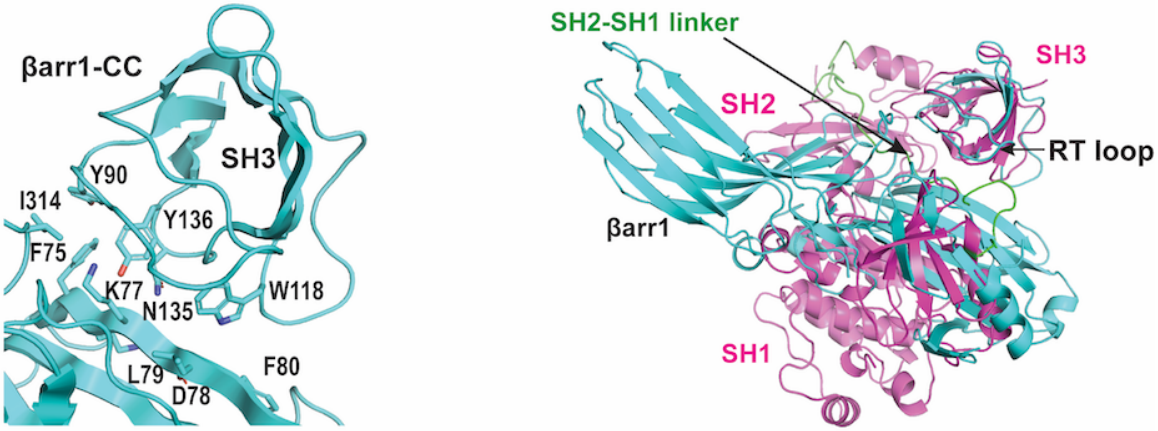

Figure S6. βarr1 binds to the aromatic surface of SH3 and releases the SH1 domain of Src.

(**A**) Left panel: structure of three-domain Src (residues 82-533, SH3-SH2-SH1) in the inactive conformation (PDB: 1FMK), cartoon representation (magenta). Middle panel: interactions of Src SH3 domain with the SH2-SH1 linker (green). Right panel: interactions of Src SH3 domain with the kinase domain and the SH3-SH2 linker; the hydrogen bonds are depicted as dashed lines.

(**B, C**) SH3–βarr1-N (B) (yellow) and SH3–βarr1-CC (C) (cyan) interfaces and structural superpositions with inactive Src (magenta). Note that binding to βarr1 displaces the SH2-SH1 linker (green) of Src.

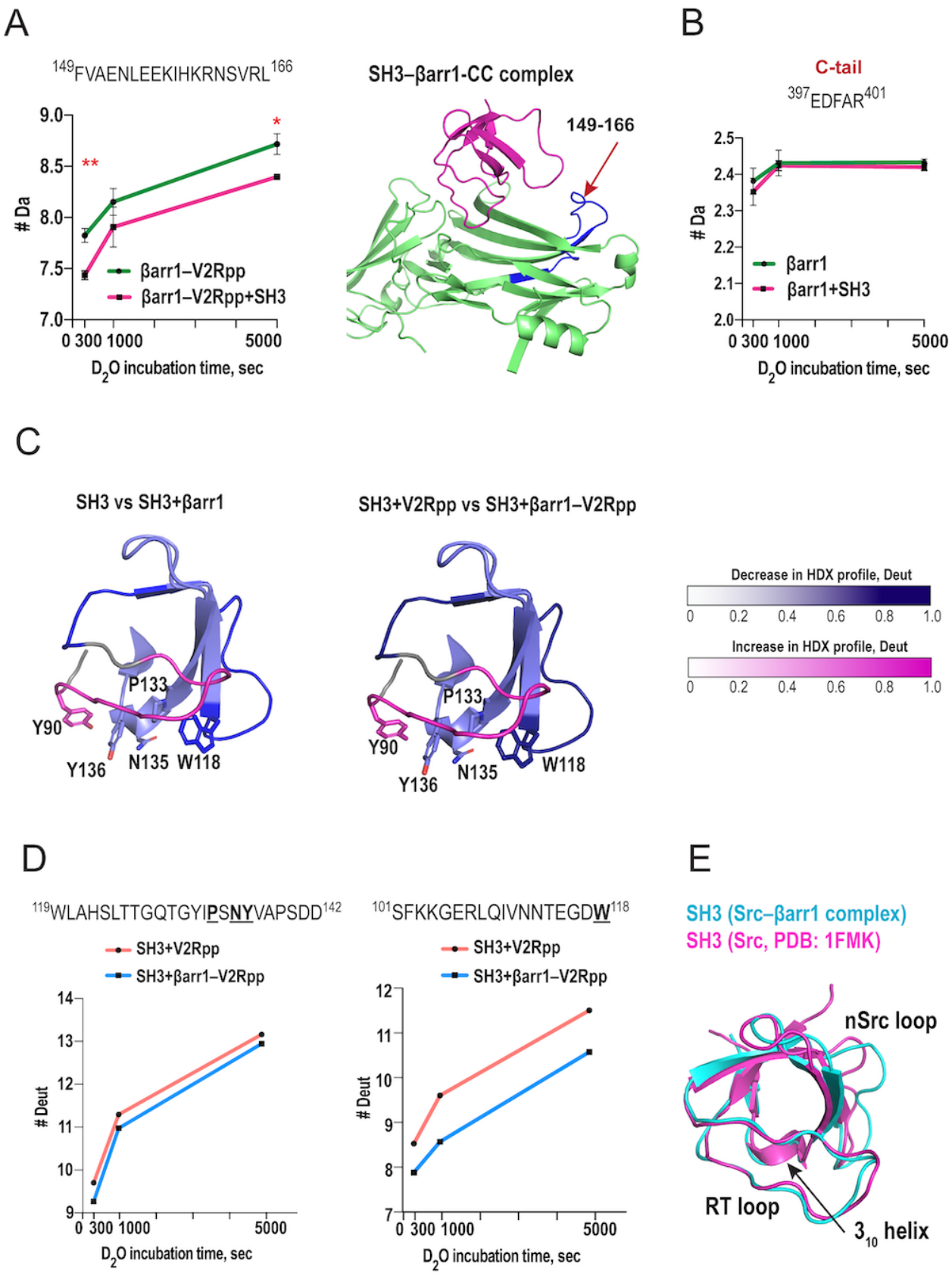

Figure S7. HDX profile changes in βarr1 and SH3 upon co-incubation

(**A**) Left panel: The HDX profile of βarr1 residues 149-166. Data represent the mean ± standard deviation (SD) of three independent experiments. Statistical analysis was performed using Student's t-test (*$p < 0.05$, **$p < 0.01$). Right panel: Structure of SH3–βarr1-CC complex, focus on region ^{149}FVAENLEEKIHKRNSVRL^{166} (red arrow) located in close proximity to SH3. (**B**) The HDX profile of βarr1 C-tail shows no changes in deuterium uptake in the presence of SH3 (βarr1, green; SH3–βarr1, magenta). (**C**) HDX profile changes in SH3 (PDB: 2PTK) upon co-incubation with free βarr1 (left panel) or V2Rpp-activated βarr1 (right panel). Regions with decreased and increased deuterium uptake are shaded in blue and magenta, respectively. Only regions that showed differences between the states in deuterium uptake (>0.2 Da) in at least two overlapping peptides are indicated. (**D**) The HDX profile of corresponding peptides in SH3. (**E**) Structural superposition of SH3 domains in Src–βarr1 complex (cyan) and in the crystal structure of Src (PDB: 1FMK, magenta).

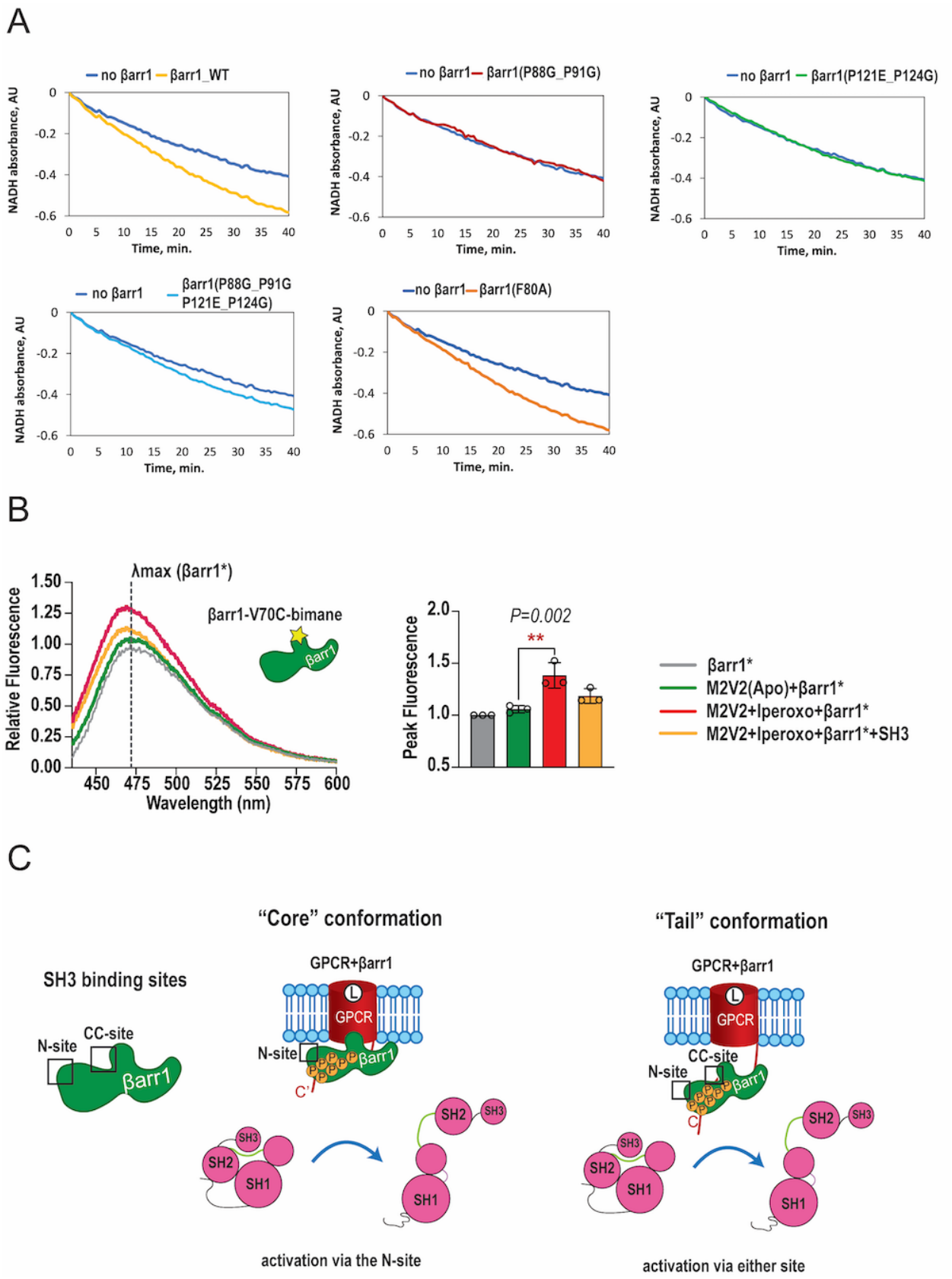

Figure S8. Physiological roles of SH3-binding sites of βarr1

(A) Representative progress curves of NADH oxidation coupled to peptide phosphorylation by Src alone and in the presence of βarr1 WT or βarr1 mutant measured by continuous kinase colorimetric assay. The higher rate of NADH oxidation corresponds to higher Src activity. (**B**) SH3 binding interferes with the core coupling of βarr1 to the phosphorylated chimeric M2-muscarinic receptor reconstituted in MSP1D1E3 nanodiscs (M2V2). Left panel: representative experiment of βarr1 finger loop bimane fluorescence. Right panel: peak fluorescence of βarr1 finger loop bimane; individual data, mean ±SD of three independent experiments is shown. Statistical differences were determined by one-way ANOVA and Dunnett's multiple comparison test. (**C**) Schematic of GPCR–βarr1 conformational preference for Src activation.

Table S1. Cryo-EM data collection, refinement and validation statistics

	SH3_95C–βarr1_120C–V2Rpp–Fab30–Nb32 (SH3–βarr1-CC) (EMD-45977) (PDB 9CX3)	**SH3_95C–βarr1_92C–V2Rpp–Fab30 (SH3–βarr1-N)** (EMD-45982) (PDB 9CX9)	**Src_95C–βarr1_120C–V2Rpp–Fab30–Nb32 (Src–βarr1)** (EMD-44881) (PDB 9BT8)
Data collection and processing			
Magnification	81,000	81,000	81,000
Voltage (kV)	300	300	300
Electron exposure (e–/Å^2)	58.5	53.8	54.6
Defocus range (μm)	-0.8 to -2.5	-0.8 to -2.5	-0.8 to -2.5
Pixel size (Å)	1.08 (collection) 1.3824 (final)	1.08 (collection) 1.3824 (final)	1.08 (collection) 1.44 (final)
Symmetry imposed	C1	C1	C1
Initial particle projections (no.)	200,270	5,607,258	9,770,378
Final particle projections (no.)	118,020	345,529	140,156
Map resolution (Å)	3.5	3.3	3.3
FSC threshold	0.143	0.143	0.143
Map resolution range (Å)	3.1-10.6	3.1-9.5	3.2-11.3
Refinement			
Initial model used (PDB code)	6NI2	4JQI	8U7A
Model resolution (Å)	3.4	3.3	3.2
FSC threshold	0.143	0.143	0.143
Map sharpening *B* factor (Å^2)	-80.3	-83.2	-77.5
Model composition			
Non-hydrogen atoms	5675 726	4801 609	5713 728
Protein residues	0	0	0
Ligands			
B factors (Å^2)			
Protein (min/max/mean)	20.22/103.43/47.96	8.88/113.35/39.95	10.51/115.11/53.64
Ligand	---	---	
R.m.s. deviations			
Bond lengths (Å)	0.003	0.003	0.004
Bond angles (°)	0.664	0.615	0.572
Validation			
MolProbity score	1.90	1.71	1.55
Clashscore	10.50	7.44	6.88
Poor rotamers (%)	0.16	0.19	0.32
Ramachandran plot			
Favored (%)	94.84	95.70	97.00
Allowed (%)	5.16	4.30	3.00
Disallowed (%)	0.00	0.00	0.00

Table S2. Oligonucleotides and plasmids

Original construct	Mutation	Forward and reverse oligonucleotides (5'→3')	Generated plasmids
pGEX-4T1_βarr1-393_MinCys	A82C	gggaaggactgcacgttacacacaaacaggtctttgcg cgcaaagacctgtttgtgtgtaacgtgcagtccttccc	pGEX-4T1_βarr1-393_MinCys_A82C
pGEX-4T1_βarr1-393_MinCys	F87C	gtggctaacgtgcagtcctgcccaccggcccctgaggacaag cttgtcctcaggggccggtgggcaggactgcacgttagccac	pGEX-4T1_βarr1-393_MinCys_F87C
pGEX-4T1_βarr1-393_MinCys	P88C	gtcctcaggggccgggcagaaggactgcacgtt aacgtgcagtccttctgcccggcccctgaggac	pGEX-4T1_βarr1-393_MinCys_P88C
pGEX-4T1_βarr1-393_MinCys	P89C	gtggctaacgtgcagtccttcccatgcgcccctgaggacaagaagccactgact agtcagtggcttcttgtcctcaggggcgcatgggaaggactgcacgttagccac	pGEX-4T1_βarr1-393_MinCys_P89C
pGEX-4T1_βarr1-393_MinCys	A90C	ttcttgtcctcagggcacggtgggaaggactg cagtccttcccaccgtgccctgaggacaagaa	pGEX-4T1_βarr1-393_MinCys_A90C
pGEX-4T1_βarr1-393_MinCys	P91C	gcttcttgtcctcacaggccggtgggaagg ccttcccaccggcctgtgaggacaagaagc	pGEX-4T1_βarr1-393_MinCys_P91C
pGEX-4T1_βarr1-393_MinCys	E92C	tcagtggcttcttgtcgcaaggggccggtgggaag cttcccaccggccccttgcgacaagaagccactga	pGEX-4T1_βarr1-393_MinCys_E92C
pGEX-4T1_βarr1-393_MinCys	D93C	gtcagtggcttcttgcactcaggggccggtgg ccaccggcccctgagtgcaagaagccactgac	pGEX-4T1_βarr1-393_MinCys_D93C
pGEX-4T1_βarr1-393_MinCys	K94C	ccgagtcagtggcttgcagtcctcaggggccgg ccggcccctgaggactgcaagccactgactcgg	pGEX-4T1_βarr1-393_MinCys_K94C
pGEX-4T1_βarr1-393_MinCys	K95C	gtagccgagtcagtgggcacttgtcctcaggggcc ggcccctgaggacaagtgcccactgactcggctac	pGEX-4T1_βarr1-393_MinCys_K95C
pGEX-4T1_βarr1-393_MinCys	P96C	ccaccggcccctgaggacaagaagtgcctgactcggctacaagagcgactc gagtcgctcttgtagccgagtcaggcacttcttgtcctcaggggccggtgg	pGEX-4T1_βarr1-393_MinCys_P96C
pGEX-4T1_βarr1-393_MinCys	Y113C	gtgaaggggcaggcatgctcgcccagc gctgggcgagcatgcctgccccttcac	pGEX-4T1_βarr1-393_MinCys_Y113C
pGEX-4T1_βarr1-393_MinCys	P114C	gatctcaaaggtgaagcagtaggcatgctcgccc gggcgagcatgcctactgcttcacctttgagatc	pGEX-4T1_βarr1-393_MinCys_P114C
pGEX-4T1_βarr1-393_MinCys	T116C	gcgagcatgcctacccctctgctttgagatcccgccaaacc ggtttggcgggatctcaaagcagaaggggtaggcatgctcgc	pGEX-4T1_βarr1-393_MinCys_T116C
pGEX-4T1_βarr1-393_MinCys	E118C	ggcgagcatgcctacccctcaccttttgcatcccgccaaaccttccgagctcagtc gactgagctcggaaggtttggcgggatgcaaaaggtgaaggggtaggcatgctcgcc	pGEX-4T1_βarr1-393_MinCys_E118C
pGEX-4T1_βarr1-393_MinCys	P120C	tgagctcggaaggtttgggcagatctcaaaggtgaaggg cccttcacctttgagatctgcccaaaccttccgagctca	pGEX-4T1_βarr1-393_MinCys_P120C
pGEX-4T1_βarr1-393_MinCys	P121C	tgactgagctcggaaggttgcacgggatctcaaaggtgaag cttcacctttgagatcccgtgcaaccttccgagctcagtca	pGEX-4T1_βarr1-393_MinCys_P121C
pGEX-4T1_βarr1-393_MinCys	N122C	ctgagctcggaaggcatggcgggatctcaaagg cctttgagatcccgccatgccttccgagctcag	pGEX-4T1_βarr1-393_MinCys_N122C

pET-28a_SH3	L89C	gggactcgtagtcatagcaagccacgaaagtggtgac gtcaccactttcgtggcttgctatgactacgagtcccg	pET-28a_SH3_L89C
pET-28a_SH3	Y90C	gactcgtagtcacagagagccacgaaagtggtgacc ggtcaccactttcgtggctctctgtgactacgagtc	pET-28a_SH3_Y90C
pET-28a_SH3	Y92C	ccgggactcgcagtcatagagagccacgaa ttcgtggctctctatgactgcgagtcccgg	pET-28a_SH3_Y92C
pET-28a_SH3	R95C	ggacaagtccgtttcagtgcaggactcgtagtcatagag ctctatgactacgagtcctgcactgaaacggacttgtcc	pET-28a_SH3_R95C
pET-28a_SH3	E115C	gagccagccaccagtcaccgcacgtgttgttgacaatctgc gcagattgtcaacaacacgtgcggtgactggtggctggctc	pET-28a_SH3_E115C
pET-28a_SH3	D117C	gaatgagccagccaccagcaaccttccgtgttgttgac gtcaacaacacggaaggttgctggtggctggctcattc	pET-28a_SH3_D117C
pET-28a_SH3	W118C	gaatgagccagccagcagtcaccttccgt acggaaggtgactgctggctggctcattc	pET-28a_SH3_W118C
pET-28a_SH3	Y131C	tagttactggggatgcagcccgtctgtcctg caggacagacgggctgcatccccagtaacta	pET-28a_SH3_Y131C
pET-28a_SH3	P133C	gcgcgacatagttactgcagatgtagcccgtctgtc gacagacgggctacatctgcagtaactatgtcgcgc	pET-28a_SH3_P133C
pET-28a_SH3	S134C	cgcgacatagttacaggggatgtagcccg cgggctacatcccctgtaactatgtcgcg	pET-28a_SH3_P134C
pET-28a_SH3	N135C	gagggcgcgacatagcaactggggatgtagcc ggctacatccccagttgctatgtcgcgccctc	pET-28a_SH3_N135C
pET-28a_SH3	Y136C	gggcgcgacacagttactggggatgtagcc ggctacatccccagtaactgtgtcgcgccc	pET-28a_SH3_Y136C
pET-28a_SH3	A138C	cctggatctagtctgaggggcagacatagttactggggatg catccccagtaactatgtctgcccctcagactagatccagg	pET-28a_SH3_A138C
pET-28a_SH3-FLAG	Y90A	ccgggactcgtagtcagcgagagccacgaaagtg cactttcgtggctctcgctgactacgagtcccgg	pET-28a_SH3-FLAG_Y90A
pET-28a_SH3-FLAG	Y92C	ccgggactcgcagtcatagagagccacgaa ttcgtggctctctatgactgcgagtcccgg	pET-28a_SH3-FLAG_Y92C
pET-28a_SH3-FLAG_Y90A / pET-28a_SH3-FLAG_Y92C	Y136A	gagggcgcgacagcgttactggggatgtagcc ggctacatccccagtaacgctgtcgcgccctc	pET-28a_SH3-FLAG_Y90A_Y136A/ pET-28a_SH3-FLAG_Y92C_Y136A
pET-28a_SH3-FLAG_Y92C_Y136A	W118A	ggaatgagccagccacgcgtcaccttccgtgttg caacacggaaggtgacgcgtggctggctcattcc	pET-28a_SH3-FLAG_Y92C_W118A_Y136A
pET-28a_Src	C185S	aacggagaggctataggcacctttgtcgtctc gagacgacaaaaggtgcctatagcctctccgtt	pET-28a_Src_C185S
pET-28a_Src_C185S	C238S	gtcaggcggtggctcaagccatcagca tgctgatggcttgagccaccgcctgac	pET-28a_Src_C185S_C238S

pET-28a_Src_C185S_C238S	C245V	gcttggacgtggggacgacgttggtcaggc gcctgaccaacgtcgtccccacgtccaagc	pET-28a_Src_C185S_C238S_C245V
pET-28a_Src_C185S_C238S_C245V	C277S	cctctccaaagctgccctgccccag ctggggcagggcagctttggagagg	pET-28a_Src_C185S_C238S_C245V_C277S
pET-28a_Src_C185S_C238S_C245V_C277S	C400S	gtcagccaccttgctcaccaggttctccc gggagaacctggtgagcaaggtggctgac	pET-28a_Src_C185S_C238S_C245V_C277S_C400S
pET-28a_Src_C185S_C238S_C245V_C277S_C400S	R95C	ggacaagtccgtttcagtgcaggactcgtagtcatagag ctctatgactacgagtcctgcactgaaacggacttgtcc	pET-28a_Src_C185S_C238S_C245V_C277S_C400S_R95C
pcDNA3_βarr1-HA / pGEX-4T1_βarr1	P88G-P91G	cttcttgtcctcaccggccggtccgaaggactgcacg cgtgcagtccttcggaccggccggtgaggacaagaag	pcDNA3_βarr1-HA_P88G_P91G / pGEX-4T1_βarr1_P88G_P91G
pcDNA3_βarr1-HA/ pGEX-4T1_βarr1	P121E-P124G	gttgcaatgtgactgagcacccaaggttctccgggatctcaaaggtgaagg ccttcacctttgagatcccggagaaccttgggtgctcagtcacattgcaac	pcDNA3_βarr1-HA_P121E_P124G / pGEX-4T1_βarr1_P121E_P124G
pcDNA3_βarr1-HA / pGEX-4T1_βarr1	F80A	ggactgcacgttagccacagccaggtctttgcgaaaagtc gacttttcgcaaagacctggctgtggctaacgtgcagtcc	pcDNA3_βarr1-HA_F80A / pGEX-4T1_βarr1_F80A
pcDNA3_βarr1-HA_P121E_P124G / pGEX-4T1_βarr1_P121E_P124G	P88G-P91G	cttcttgtcctcaccggccggtccgaaggactgcacg cgtgcagtccttcggaccggccggtgaggacaagaag	pcDNA3_βarr1-HA_P88G_P91G_P121E_P124G / pGEX-4T1_βarr1_P88G_P91G_P121E_P124G

Movie S1. SH3–βarr1-CC complex, cryo-EM map and model colored by subunit (green, βarr1; magenta, SH3; red, V2Rpp; blue, Fab30; yellow, Nb32). Interacting residues are shown as sticks, hydrogen bonds are indicated as dashed lines. Map contour level is 0.40.

Movie S2. SH3–βarr1-N complex, cryo-EM map and model colored by subunit (green, βarr1; magenta, SH3; red, V2Rpp; blue, Fab30). Interacting residues are shown as sticks. Map contour level is 0.40.

Movie S3. βarr1 activates Src by SH3 domain displacement. Inactive Src (magenta) is constrained by the intramolecular interactions between SH3, SH2 and SH1 domains. βarr1 (green, the βarr1-CC site is shown) binds the aromatic surface of SH3 and displaces the SH2-SH1 linker (yellow) releasing the catalytic (SH1) domain of Src.

Materials and Methods

Bacterial strains

Escherichia coli strain DH5α (C2987, New England Biolabs) was used for plasmid propagation.

Protein expression was done in *E. coli* BL21 derivative strain (C3010, New England Biolabs).

Cell culture

Human embryonic kidney CRISPR-Cas9-based βarr1/βarr2 double knock-out cell line (HEK-293 βarr1/βarr2 dKO) (*36*) was maintained in Gibco Minimum Essential Media (MEM) supplemented with 1% penicillin-streptomycin and 10% (v/v) fetal bovine serum at 37 °C and 5% CO_2.

Molecular biology

Bacterial expression constructs for wild-type (residues 2-418) and a minimal cysteine (C59A, C125S, C140I, C150V, C242V, C251V, and C269S) and truncated (βarr1–MC-393) variants of rat βarr1 (*53*), Fab30 (*54*), and Nb32 (*29*) have been reported previously. Plasmid pET28a-3D-Src expressing SH3, SH2 and SH1 domains of chicken Src (residues 83-533) and plasmid expressing YopH phosphatase were generous gifts from Prof. John Kuriyan. For structural studies Src-5Cys mutant (C185S, C238S, C245S, C277S, C400S) was generated. Plasmid expressing the SH3 domain of Src (residues 83-141) was designed by inserting a C-terminal FLAG-tag and a stop codon in pET28a-3D-Src. Mammalian expression constructs for human FLAG-M2 muscarinic receptor with C-terminal sortase ligation consensus sequence (LPETGGH) and 6×His-tag (*53*), chimeric FLAG-β2-adrenergic receptor with C-terminal tail of vasopressin 2 receptor (*55*), SNAP-vasopressin 2 receptor (V2R) (*56*), HA-tagged βarr1 (*4*), and human Src (*4*) have been previously reported and functionally verified. Mammalian expression construct for FLAG-dopamine 1 receptor (FLAG-D1R) was a generous gift from Dr. Sudarshan Rajagopal. Mutations were introduced using QuickChange II site-directed mutagenesis kit (Agilent) and verified by Sanger sequencing. Oligonucleotides sequences are provided in Table S2.

Protein expression and purification

The expression and purification of Src from *Escherichia coli* are described in detail elsewhere (*57*). Src construct (residues 83-533) without the N-terminal disordered region was used for the structural and *in vitro* studies. Briefly, Src was co-expressed with YopH phosphatase and purified by immobilized metal ion affinity chromatography and anion exchange chromatography. The SH3 domain of Src and its variants were purified by immobilized metal ion affinity chromatography and size exclusion chromatography (SEC). Wild-type βarr1 and its variants (*58*), Fab30 (*59*), and Nb32 (*29*) were expressed and purified as described previously. The expression and purification of FLAG-M2 receptor containing a C-terminal sortase ligation consensus sequence (LPETGGH), sortase ligation reaction and reconstitution in MSP1D1E3 nanodiscs are described elsewhere (*11, 53*).

Disulfide trapping

βarr1–MC-393 mutant (30 μM) was incubated with 3-fold molar excess of V2Rpp, 1.5 molar excess of Fab30, and 2-fold molar excess of SH3 mutant or Src mutant in 20 mM HEPES 7.5, 150 mM NaCl buffer for 30 minutes at room temperature. The disulfide trapping reactions were initiated by 1 mM H_2O_2. After 1-hour incubation at room temperature the reactions were terminated by addition of 4x Laemmli sample buffer (without β-mercaptoethanol) (BioRad), subjected to SDS-PAGE, visualized by Ready Blue Coomassie stain (Sigma-Aldrich) and quantified by *ImageJ v1.52a*. The band of SH3–βarr1 complex (~60 kDa) or Src–βarr1 (~130 kDa) was normalized to the total density of all bands in each sample. To test the effect of V2Rpp and Fab30 on formation of disulfide trapped complexes, the reactions were performed as described above; in reactions without V2Rpp and Fab30 the equivalent amount of buffer was added. The

samples were subjected to SDS-PAGE and Western blotting, detected by polyclonal A1CT antibody generated in Lefkowitz lab (*60*) (1:5000) for βarr1.

Formation of SH3–βarr1 and Src–βarr1 complexes

The βarr1–MC-393 mutant (100 μM) was incubated with 2-fold molar excess of the SH3 mutant or Src mutant for 30 minutes at room temperature, followed by disulfide trapping as described above. SH3–βarr1 was separated from unbound βarr1 by immobilized metal ion affinity chromatography using Talon resin (Takara Bio). Src–βarr1 was separated from unbound βarr1 and Src by SEC. SH3–βarr1 and Src–βarr1 complexes were then incubated with 3-fold molar excess of V2Rpp, 1.5-fold molar excess of Fab30, 2-fold molar excess of Nb32 (for SH3–βarr1-CC and Src–βarr1) for 30 minutes at room temperature. The complexes were subjected to SEC on a Superdex 200 Increase column (Cytiva Life Sciences) in 20 mM HEPES 7.5, 150 mM NaCl buffer. Peak fractions were concentrated to 6-8 mg/ml using Vivaspin® 6 column with molecular weight cut-off of 30,000 kDa (Sartorius).

Cryo-EM grid preparation and data acquisition

In the preliminary cryo-EM experiments, we observed that the complexes exhibited strong preferred orientation in vitreous ice. To alleviate the preferred orientation problem, 8 mM CHAPSO was added to the sample immediately before vitrification (*61*). The sample was applied to glow-discharged 300-mesh holey-carbon grids (Quantifoil R1.2/1.3, Electron Microscopy Sciences) or gold grids (Ultrafoil R0.6/1.0, Electron Microscopy Sciences) and vitrified using a Vitrobot Mark IV (Thermo Fisher Scientific) at 4 °C and 100% humidity. The data were collected on a Titan Krios transmission electron microscope (Thermo Fisher) operating at 300 kV equipped with a K3 direct electron detector (Gatan) in counting mode with a BioQuantum GIF energy filter (slit width of 20 eV) at a magnification of ×81,000 corresponding to a pixel size of 1.08 Å at the specimen level. 60-frame movies with a dose rate of ~15 electrons per pixel per second and a total accumulated dose of ~53-60 electrons per $Å^2$ were collected using the *Latitude-S* (Gatan) single-particle data acquisition program. The nominal defocus values were set from −0.8 to −2.5 μm.

Cryo-EM data processing

Movies were subjected to beam-induced motion correction using Patch Motion Correction in *CryoSPARC v4.0.1* (*62*) followed by determination of Contrast transfer function (CTF) parameters in Patch CTF. Micrographs with CTF fit better than 3.5 Å were used for further analysis. Particles manually selected from 15 micrographs were used to train a model in the particle picking tool *Topaz v0.2.5a* (*63*). The trained model was used to pick particles in all micrographs generating 200,270 particle projections for the SH3–βarr1-CC complex and 760,233 particle projections for the SH3–βarr1-N complex. The particles were rescaled to the pixel size of 1.3824 Å for further processing. For the SH3–βarr1-CC complex, the particle stack was subjected to 2D classification, *Ab Initio* model generation, non-uniform refinement and local refinement with a mask excluding the constant (CL/CH1) region of Fab30 (FabCR) in *CryoSPARC*. Particles were then imported to *RELION v3.1* (*64*) and subjected to 3D classification without alignment with a mask excluding the constant (CL/CH1) region of Fab30 (FabCR). Classes showing a clearly defined density for the SH3 domain (118,020 particles) were re-imported to *CryoSPARC* and subjected to local refinement with a mask on FabCR and a fulcrum on the SH3–βarr1 interface generating a map with a global resolution of 3.5 Å at a Fourier shell correlation of 0.143 (fig. S1A, S2A, S2C). For the SH3–βarr1-N complex, the particles picked with *Topaz* were subjected to 2D classification and the best 2D classes were used in template picking (5,607,258 particles). A subset of particles (1,000,000) was used to generate six *Ab Initio* classes. All particles were then subjected to four

rounds of heterogeneous refinement. The resulting particle stack (345,529) was used in non-uniform refinement and local refinement with a mask excluding FabCR generating a map with a global resolution of 3.3 Å at a Fourier shell correlation of 0.143 (fig. S1B, S2B, S2D). For Src–βarr1 complex the particles picked with *Topaz* (94,196 particles) were subjected to 2D classification and the best 2D classes were used in template picking (9,770,378 particles). The particles were rescaled to the pixel size of 1.44 Å for further processing. A subset of particles (1,000,000) was used to generate three *Ab Initio* classes. All particles were then subjected to three rounds of heterogeneous refinement, followed by non-uniform refinement and local refinement with a mask excluding FabCR. The resulting particle stack (692,850) was subjected to 3D classification without alignment in *CryoSPARC* and then in *RELION* with a mask excluding FabCR. Finally, the best class with 140,156 particles was subjected to another round of local refinement in *CryoSPARC,* generating a map with a global resolution of 3.3 Å (fig. S4C, fig. S5A-S5B).

Model building and refinement

Cryo-EM maps for SH3–βarr1 complexes were post-processed using DeepEMhancer (*65*) to improve the interpretability of maps, specifically in the βarr1 loops and at the SH3–βarr1 interface. Since the overall resolution of maps was better than 4 Å, highRes deep learning model was used during DeepEMhancer processing of maps. The initial models of the SH3–βarr1-CC complex and Src–βarr1 complex were built manually by fitting the crystal structures of SH3 (PDB: 2PTK), βarr1–V2Rpp–Fab30–Nb32 complex (PDB code: 6NI2) into the experimental electron densities using *UCSF Chimera v1.15* (*66*). The structures were refined by combining manual adjustments in *Coot v0.9.8.3 (67)* and ISOLDE (*68*) in *UCSF ChimeraX 1.6.1 (69)*, followed by real-space refinement in *PHENIX v1.20.1-4487 (70)* with Ramachandran, rotamer, torsion, and secondary structure restraints enforced. For the SH3–βarr1-N complex, the crystal structure of the βarr1–V2Rpp–Fab30 complex (PDB code: 4JQI) was first built manually into the density and refined similarly to the SH3–βarr1-CC complex. After the refinement, SH3 (PDB: 2PTK) was docked into the density guided by the position of the disulfide bond between βarr1_E92C and SH3_R95C. The rigid body fitted SH3–βarr1-N model generated above was then subjected to molecular dynamics flexible fitting (MDFF) using Cryo fit (*71*), integrated in Phenix software suite and Namdinator (*72*) followed by further iterative rounds of model building and real space refinement in *Coot v0.9.8.3 (67)* and *PHENIX v1.20.1-4487 (70).* The models were validated with *MolProbity v4.5.1 (73).* Refinement statistics are given in Table S1.

Hydrogen-deuterium exchange mass-spectrometry (HDX-MS)

To analyze the solvent accessibility of βarr1, βarr1–MC-393 (20 μM) or βarr1–MC-393–V2Rpp (20 uM βarr1; 100 uM V2Rpp) were incubated with 5-fold molar excess of SH3 in the 20 mM HEPES 7.5, 100 mM NaCl buffer for 30 minutes on ice. To test the solvent accessibility of SH3, SH3 (20 uM) was incubated with 5-fold molar excess of βarr1–MC-393 or βarr1–MC-393–V2Rpp in the 20 mM HEPES 7.5, 100 mM NaCl buffer for 30 minutes on ice. The protein stock solution was diluted 17-fold in the 20 mM HEPES 7.5, 100 mM NaCl buffer prepared in D_2O. At a designated time point (300, 1000, and 5000 s), the exchange was quenched by adding an equal volume of 0.8% formic acid in H2O, yielding pH 2.6. The sample was digested on Enzymate BEH Pepsin column (Waters) at a flow rate of 0.15 ml/min using 0.15% formic acid/3% acetonitrile as the mobile phase. An inline 4-μl C8-Opti-lynx II trap cartridge (Optimize Technologies) was used for desalting of the digested peptides. The peptides were then eluted through a C-18 column (Thermo Fisher Scientific, 50 × 1 mm Hypersil Gold C-18) using a rapid gradient from 10 to 90% acetonitrile containing 0.15% formic acid and a flow rate of 0.04 ml/min, leading directly into a

maXis-II ETD ESI-QqTOF mass spectrometer (Bruker Daltonics). The total time for the digest and desalting was 3 min, and all peptides had eluted from the C-18 column by 15 min. Pepsin and C-18 column were thoroughly washed after each run. The peptide fragments were identified using *Bruker Compass* and *Biotools* software packages. The level of deuterium incorporation was calculated using *HDExaminer-3* (Trajan Scientific) from triplicate measurements of each time point.

M2-FLAG pull-down assay

βarr1 (20 μM) was incubated with 3-fold molar excess of V2Rpp for 30 minutes at room temperature, then 10 μM of SH3-FLAG was added. 30 ul of anti-FLAG M2 affinity gel (Millipore Sigma) was added thereafter and the mixture was incubated for 1 hour at room temperature with rotation. After incubation the anti-FLAG M2 resin was collected by centrifugation and washed with 1 ml of 20 mM HEPES pH 7.5, 100 mM NaCl buffer three times. The proteins were eluted with 0.2 mg/ml FLAG-peptide in 20 mM HEPES pH 7.5, 100 mM NaCl buffer, then mixed with Laemmli sample buffer (BioRad), subjected to SDS-PAGE and Western blotting and detected by monoclonal ANTI-FLAG M2-peroxidase (HRP) antibody (1:2000) (A8592, Sigma-Aldrich, RRID: AB_439702) for SH3-FLAG and polyclonal A1CT antibody (*60*) (1:5000) for βarr1.

***In vitro* Src continuous colorimetric kinase assay**

Continuous colorimetric kinase assay was performed as previously described (*8, 74*). The reactions were performed in 100 mM HEPES 7.5, 150 mM NaCl, 5 mM MgCl2, 0.005% Triton X-100, containing 0.25 mM optimal Src peptide (AEEEIYGEFEAKKKK), 1 mM phosphoenolpyruvate, 0.3 mM NADH, 4 units of pyruvate kinase and 6 units of lactic dehydrogenase. The concentration of Src was 20 nM, the concentrations of βarr1 and V2Rpp were 100 nM and 200 nM, respectively. Reactions were started by the addition of ATP to a final concentration of 0.1 mM, and the decrease in NADH absorbance was monitored over 40 min at 25° C using a CLARIOstar microplate reader (BMG Labtech). The initial velocity of the reaction (V0) determined using a linear regression curve fit (*GraphPad Prism v9*) and was converted to the amount of product formed in the reaction volume per minute using the Beer-Lambert law. Statistical comparisons were determined by one-way ANOVA and Dunnett's multiple comparison test.

Src activation assay in HEK-293 βarr1/βarr2 dKO cells

HEK-293 βarr1/βarr2 dKO cells (*36*) were co-transfected with receptor (FLAG-D1R or chimeric FLAG-β2V2), Src (only for chimeric FLAG-β2V2) and wild-type or mutant βarr1 with a C-terminal HA tag with a 1:5 DNA:FuGENE®6 (Promega) ratio according to the manufacturer's instructions. All experiments were conducted 48 hours after transfection. Cells were serum starved for 16 hours in MEM supplemented with 1% penicillin-streptomycin and 0.1% (w/v) bovine serum albumin. The assay was initiated with 5-minute stimulation (10 μM dopamine for D1R) or 10-minute stimulation (10 μM BI-167107 for β2V2) at 37 °C. The medium was removed, cells were placed on ice and lysed with 2x Laemmli sample buffer (BioRad) supplemented with 4% β-mercaptoethanol. Samples of equal volume from cell lysates were separated with SDS-PAGE, transferred to nitrocellulose membranes and immunoblotted. Primary antibodies and dilution used are as follow: monoclonal ANTI-FLAG M2 peroxidase (HRP) antibody (1:2000) (A8592, Sigma-Aldrich, RRID: AB_439702) to detect β2V2, polyclonal A1CT antibody generated in Lefkowitz lab (*60*) (1:5000) for wild-type and mutant βarr1, anti-Src monoclonal antibody (1:1000) (MA5-15214, Thermo Fisher Scientific, RRID: AB_10980540) for total Src, anti-Src polyclonal Y418 for overexpressed Src (1:5000) (ab4816, Abcam, RRID: AB_304652), and Phospho-Src family polyclonal Y416 for endogenous Src (1:10000) (2101, Cell Signaling, RRID: AB_331697).

Secondary antibodies included HRP conjugated anti-rabbit (NA934, Cytiva Life Sciences, RRID: AB_772206) and anti-mouse (NA931, Cytiva Life Sciences, RRID: AB_772210). Western Blot images were taken using BioRad ChemiDoc system and the densitometry analysis was performed by *ImageJ v1.52a* and *ImageLab v6.1.*

Bimane fluorescence

Purified βarr1-MC-393 V70C was labeled with monobromobimane (mBr) (Sigma-Aldrich), as described previously (*11*). The experiments were performed using membranes with phosphorylated vasopressin 2 receptor (V2R) and purified chimeric M2-muscarinic receptor (M2V2) reconstituted in lipid nanodiscs. Expi-293 cells grown in suspension were co-transfected with plasmids expressing the human V2R and the membrane targeted form of GRK2. Transfected cells were grown in suspension for 48h and thereafter were stimulated with AVP (100 nM) for 30 min at 37°C followed by harvesting by centrifugation at 4°C. Cell pellets were washed with cold HBSS, snap frozen in liquid N2 and stored at -80°C prior to preparation of crude membranes as described previously (*75*). Aliquots of phosphorylated V2R membranes were activated with AVP (10μM) then incubated with βarr1 V70C-mBr (20 nM), and SH3 (250 nM) in the assay buffer (20 mM HEPES 7.4, 100 mM NaCl, 1 mg/ml bovine serum albumin) for 120 min at room temperature in black solid-bottom 96-well microplates (Corning) with gentle agitation. Purified M2V2 reconstituted in lipid nanodiscs (25 nM) was activated with 10 μM iperoxo, and subsequently incubated for 60 min at room temperature with 1.5-fold molar access of bimane-labeled βarr1, 2-fold molar excess of Fab30 and SH3 (500 nM). Fluorescence emission spectra were collected in top-read mode, with excitation at 370 nm (16 nm bandpass) and emission scanning from 410 nm to 640 nm (10 nm bandpass) in 0.5 nm increments using a CLARIOstar microplate reader (BMG Labtech). Statistical comparisons were determined by comparing the area under the curves (*GraphPad Prism v9*) and peak fluorescence using one-way ANOVA and Dunnett's multiple comparison test from three (M2V2) or six (V2R membranes) independent experiments.

Isothermal titration calorimetry (ITC)

ITC measurements were performed using the MicroCal PEAQ-ITC system (Malvern). Purified βarr1–V2Rpp and SH3 were dialyzed in 20 mM HEPES, pH 7.5, 100 mM NaCl. 75 μM of βarr1–V2Rpp was loaded into the sample cell and 750 μM of SH3 into the injection syringe. The system was equilibrated to 25 °C. Titration curves were initiated by a 0.4 μL injection from syringe, followed by 2.0 μL injections (at 180 s intervals) into the sample cell. During the experiment, the reference power was set to 7 μcal·s-1 and the sample cell was stirred continuously at 750 rpm. Raw data, excluding the peak from the first injection, were baseline corrected, peak area integrated, and normalized. Data were analyzed using *MicroCal Origin* software to obtain thermodynamic parameters of binding and association constant (Ka=1/Kd).

Data and statistical analysis

Data were analyzed using *GraphPad Prism v9*. Data represent the mean ±SD of at least three independent experiments. Statistical significance for more than two groups were determined by a one-way ANOVA and Dunnett's multiple comparison test. Statistical significance for two groups was determined by Student's t-test. No samples or data points were excluded from analysis.

References and Notes

1. P. H. McDonald, R. J. Lefkowitz, Beta-Arrestins: new roles in regulating heptahelical receptors' functions. *Cell Signal* **13**, 683-689 (2001).
2. R. J. Lefkowitz, Arrestins come of age: a personal historical perspective. *Prog Mol Biol Transl Sci* **118**, 3-18 (2013).
3. Y. K. Peterson, L. M. Luttrell, The Diverse Roles of Arrestin Scaffolds in G Protein-Coupled Receptor Signaling. *Pharmacol Rev* **69**, 256-297 (2017).
4. L. M. Luttrell *et al.*, Beta-arrestin-dependent formation of beta2 adrenergic receptor-Src protein kinase complexes. *Science* **283**, 655-661 (1999).
5. P. H. McDonald *et al.*, Beta-arrestin 2: a receptor-regulated MAPK scaffold for the activation of JNK3. *Science* **290**, 1574-1577 (2000).
6. L. M. Luttrell *et al.*, Activation and targeting of extracellular signal-regulated kinases by beta-arrestin scaffolds. *Proc Natl Acad Sci U S A* **98**, 2449-2454 (2001).
7. F. Yang *et al.*, Allosteric mechanisms underlie GPCR signaling to SH3-domain proteins through arrestin. *Nature Chemical Biology* **14**, 876-+ (2018).
8. N. Pakharukova, A. Masoudi, B. Pani, D. P. Staus, R. J. Lefkowitz, Allosteric activation of proto-oncogene kinase Src by GPCR-beta-arrestin complexes. *J Biol Chem* **295**, 16773-16784 (2020).
9. Y. Zang, A. W. Kahsai, N. Pakharukova, L. Y. Huang, R. J. Lefkowitz, The GPCR-beta-arrestin complex allosterically activates C-Raf by binding its amino terminus. *J Biol Chem* **297**, 101369 (2021).
10. A. W. Kahsai *et al.*, Signal transduction at GPCRs: Allosteric activation of the ERK MAPK by β-arrestin. *P Natl Acad Sci USA* **120**, (2023).
11. D. P. Staus *et al.*, Structure of the M2 muscarinic receptor-beta-arrestin complex in a lipid nanodisc. *Nature* **579**, 297-302 (2020).
12. W. Huang *et al.*, Structure of the neurotensin receptor 1 in complex with beta-arrestin 1. *Nature* **579**, 303-308 (2020).
13. Y. Lee *et al.*, Molecular basis of beta-arrestin coupling to formoterol-bound beta(1)-adrenoceptor. *Nature* **583**, 862-+ (2020).
14. J. Bous *et al.*, Structure of the vasopressin hormone-V2 receptor-beta-arrestin1 ternary complex. *Sci Adv* **8**, eabo7761 (2022).
15. J. Teyra *et al.*, Comprehensive Analysis of the Human SH3 Domain Family Reveals a Wide Variety of Non-canonical Specificities. *Structure* **25**, 1598-1610 e1593 (2017).
16. S. Karkkainen *et al.*, Identification of preferred protein interactions by phage-display of the human Src homology-3 proteome. *EMBO Rep* **7**, 186-191 (2006).
17. C. H. Lee, K. Saksela, U. A. Mirza, B. T. Chait, J. Kuriyan, Crystal structure of the conserved core of HIV-1 Nef complexed with a Src family SH3 domain. *Cell* **85**, 931-942 (1996).
18. J. J. Alvarado, S. Tarafdar, J. I. Yeh, T. E. Smithgall, Interaction with the Src homology (SH3-SH2) region of the Src-family kinase Hck structures the HIV-1 Nef dimer for kinase activation and effector recruitment. *J Biol Chem* **289**, 28539-28553 (2014).
19. Y. He, L. Hicke, I. Radhakrishnan, Structural basis for ubiquitin recognition by SH3 domains. *J Mol Biol* **373**, 190-196 (2007).
20. J. F. Trempe *et al.*, SH3 domains from a subset of BAR proteins define a Ubl-binding domain and implicate parkin in synaptic ubiquitination. *Mol Cell* **36**, 1034-1047 (2009).

21. K. Hanawa-Suetsugu *et al.*, Structural basis for mutual relief of the Rac guanine nucleotide exchange factor DOCK2 and its partner ELMO1 from their autoinhibited forms. *P Natl Acad Sci USA* **109**, 3305-3310 (2012).
22. B. Chan *et al.*, SAP couples Fyn to SLAM immune receptors. *Nat Cell Biol* **5**, 155-160 (2003).
23. J. Vaynberg *et al.*, Structure of an ultraweak protein-protein complex and its crucial role in regulation of cell morphology and motility. *Mol Cell* **17**, 513-523 (2005).
24. T. Kaneko, L. Li, S. S. Li, The SH3 domain--a family of versatile peptide- and protein-recognition module. *Front Biosci* **13**, 4938-4952 (2008).
25. S. S. Li, Specificity and versatility of SH3 and other proline-recognition domains: structural basis and implications for cellular signal transduction. *Biochem J* **390**, 641-653 (2005).
26. K. Xiao *et al.*, Functional specialization of beta-arrestin interactions revealed by proteomic analysis. *Proc Natl Acad Sci U S A* **104**, 12011-12016 (2007).
27. I. Perez *et al.*, A Model for the Signal Initiation Complex Between Arrestin-3 and the Src Family Kinase Fgr. *J Mol Biol* **434**, 167400 (2022).
28. K. Xiao *et al.*, Revealing the architecture of protein complexes by an orthogonal approach combining HDXMS, CXMS, and disulfide trapping. *Nat Protoc* **13**, 1403-1428 (2018).
29. T. J. Cahill, 3rd *et al.*, Distinct conformations of GPCR-beta-arrestin complexes mediate desensitization, signaling, and endocytosis. *Proc Natl Acad Sci U S A* **114**, 2562-2567 (2017).
30. A. K. Shukla *et al.*, Structure of active beta-arrestin-1 bound to a G-protein-coupled receptor phosphopeptide. *Nature* **497**, 137-141 (2013).
31. K. Saksela, P. Permi, SH3 domain ligand binding: What's the consensus and where's the specificity? *FEBS Lett* **586**, 2609-2614 (2012).
32. S. C. Harrison, Variation on an Src-like theme. *Cell* **112**, 737-740 (2003).
33. W. Xu, S. C. Harrison, M. J. Eck, Three-dimensional structure of the tyrosine kinase c-Src. *Nature* **385**, 595-602 (1997).
34. I. Moarefi *et al.*, Activation of the Src-family tyrosine kinase Hck by SH3 domain displacement. *Nature* **385**, 650-653 (1997).
35. J. J. Alvarado, L. Betts, J. A. Moroco, T. E. Smithgall, J. I. Yeh, Crystal structure of the Src family kinase Hck SH3-SH2 linker regulatory region supports an SH3-dominant activation mechanism. *J Biol Chem* **285**, 35455-35461 (2010).
36. M. O'Hayre *et al.*, Genetic evidence that β-arrestins are dispensable for the initiation of β-adrenergic receptor signaling to ERK. *Sci Signal* **10**, (2017).
37. C. Qi, S. Sorrentino, O. Medalia, V. M. Korkhov, The structure of a membrane adenylyl cyclase bound to an activated stimulatory G protein. *Science* **364**, 389-+ (2019).
38. L. Qin *et al.*, Structural biology. Crystal structure of the chemokine receptor CXCR4 in complex with a viral chemokine. *Science* **347**, 1117-1122 (2015).
39. D. M. Rosenbaum *et al.*, Structure and function of an irreversible agonist-beta(2) adrenoceptor complex. *Nature* **469**, 236-240 (2011).
40. K. Alexandropoulos, D. Baltimore, Coordinate activation of c-Src by SH3- and SH2-binding sites on a novel, p130(Cas)-related protein, Sin. *Gene Dev* **10**, 1341-1355 (1996).
41. R. M. Kypta, Y. Goldberg, E. T. Ulug, S. A. Courtneidge, Association between the Pdgf Receptor and Members of the Src Family of Tyrosine Kinases. *Cell* **62**, 481-492 (1990).
42. B. S. Cobb, M. D. Schaller, T. H. Leu, J. T. Parsons, Stable Association of Pp60(Src) and Pp59(Fyn) with the Focal Adhesion-Associated Protein-Tyrosine Kinase, Pp125(Fak). *Mol Cell Biol* **14**, 147-155 (1994).

43. M. R. Burnham *et al.*, Regulation of c-SRC activity and function by the adapter protein CAS. *Mol Cell Biol* **20**, 5865-5878 (2000).
44. J. D. Bjorge, A. Jakymiw, D. J. Fujita, Selected glimpses into the activation and function of Src kinase. *Oncogene* **19**, 5620-5635 (2000).
45. R. Roskoski, Src protein-tyrosine kinase structure, mechanism, and small molecule inhibitors. *Pharmacol Res* **94**, 9-25 (2015).
46. W. E. Miller *et al.*, beta-arrestin1 interacts with the catalytic domain of the tyrosine kinase c-SRC - Role of beta-arrestin1-dependent targeting of c-SRC in receptor endocytosis. *Journal of Biological Chemistry* **275**, 11312-11319 (2000).
47. S. K. Mitra, D. D. Schlaepfer, Integrin-regulated FAK-Src signaling in normal and cancer cells. *Curr Opin Cell Biol* **18**, 516-523 (2006).
48. J. L. Benovic *et al.*, Functional desensitization of the isolated beta-adrenergic receptor by the beta-adrenergic receptor kinase: potential role of an analog of the retinal protein arrestin (48-kDa protein). *Proc Natl Acad Sci U S A* **84**, 8879-8882 (1987).
49. M. J. Lohse, J. L. Benovic, J. Codina, M. G. Caron, R. J. Lefkowitz, Beta-Arrestin - a Protein That Regulates Beta-Adrenergic-Receptor Function. *Science* **248**, 1547-1550 (1990).
50. A. I. Kaya, N. A. Perry, V. V. Gurevich, T. M. Iverson, Phosphorylation barcode-dependent signal bias of the dopamine D1 receptor. *Proc Natl Acad Sci U S A* **117**, 14139-14149 (2020).
51. J. S. Gutkind, E. Kostenis, Arrestins as rheostats of GPCR signalling. *Nat Rev Mol Cell Bio* **19**, 615-616 (2018).
52. Y. Zhang, J. Skolnick, Scoring function for automated assessment of protein structure template quality. *Proteins* **57**, 702-710 (2004).
53. D. P. Staus *et al.*, Sortase ligation enables homogeneous GPCR phosphorylation to reveal diversity in beta-arrestin coupling. *Proc Natl Acad Sci U S A* **115**, 3834-3839 (2018).
54. M. Paduch *et al.*, Generating conformation-specific synthetic antibodies to trap proteins in selected functional states. *Methods* **60**, 3-14 (2013).
55. A. K. Shukla *et al.*, Visualization of arrestin recruitment by a G-protein-coupled receptor. *Nature* **512**, 218-222 (2014).
56. A. R. B. Thomsen *et al.*, GPCR-G Protein-beta-Arrestin Super-Complex Mediates Sustained G Protein Signaling. *Cell* **166**, 907-919 (2016).
57. M. A. Seeliger *et al.*, High yield bacterial expression of active c-Abl and c-Src tyrosine kinases. *Protein Sci* **14**, 3135-3139 (2005).
58. K. N. Nobles, Z. Guan, K. Xiao, T. G. Oas, R. J. Lefkowitz, The active conformation of beta-arrestin1: direct evidence for the phosphate sensor in the N-domain and conformational differences in the active states of beta-arrestins1 and -2. *J Biol Chem* **282**, 21370-21381 (2007).
59. S. S. Rizk *et al.*, Allosteric control of ligand-binding affinity using engineered conformation-specific effector proteins. *Nat Struct Mol Biol* **18**, 437-442 (2011).
60. H. Attramadal *et al.*, Beta-Arrestin2, a Novel Member of the Arrestin Beta-Arrestin Gene Family. *Journal of Biological Chemistry* **267**, 17882-17890 (1992).
61. S. Chen, J. Li, K. R. Vinothkumar, R. Henderson, Interaction of human erythrocyte catalase with air-water interface in cryoEM. *Microscopy (Oxf)* **71**, i51-i59 (2022).
62. A. Punjani, J. L. Rubinstein, D. J. Fleet, M. A. Brubaker, cryoSPARC: algorithms for rapid unsupervised cryo-EM structure determination. *Nat Methods* **14**, 290-296 (2017).
63. T. Bepler *et al.*, Positive-unlabeled convolutional neural networks for particle picking in cryo-electron micrographs. *Nature Methods* **16**, 1153-+ (2019).

64. S. H. Scheres, RELION: implementation of a Bayesian approach to cryo-EM structure determination. *J Struct Biol* **180**, 519-530 (2012).
65. R. Sanchez-Garcia *et al.*, DeepEMhancer: a deep learning solution for cryo-EM volume post-processing. *Commun Biol* **4**, 874 (2021).
66. E. F. Pettersen *et al.*, UCSF Chimera--a visualization system for exploratory research and analysis. *J Comput Chem* **25**, 1605-1612 (2004).
67. P. Emsley, B. Lohkamp, W. G. Scott, K. Cowtan, Features and development of Coot. *Acta Crystallogr D Biol Crystallogr* **66**, 486-501 (2010).
68. T. I. Croll, ISOLDE: a physically realistic environment for model building into low-resolution electron-density maps. *Acta Crystallogr D* **74**, 519-530 (2018).
69. E. F. Pettersen *et al.*, UCSF ChimeraX: Structure visualization for researchers, educators, and developers. *Protein Sci* **30**, 70-82 (2021).
70. P. D. Adams *et al.*, PHENIX: building new software for automated crystallographic structure determination. *Acta Crystallogr D Biol Crystallogr* **58**, 1948-1954 (2002).
71. D. N. Kim *et al.*, Cryo_fit: Democratization of flexible fitting for cryo-EM. *J Struct Biol* **208**, 1-6 (2019).
72. R. T. Kidmose *et al.*, Namdinator - automatic molecular dynamics flexible fitting of structural models into cryo-EM and crystallography experimental maps. *Iucrj* **6**, 526-531 (2019).
73. V. B. Chen *et al.*, MolProbity: all-atom structure validation for macromolecular crystallography. *Acta Crystallogr D Biol Crystallogr* **66**, 12-21 (2010).
74. S. C. Barker *et al.*, Characterization of pp60c-src tyrosine kinase activities using a continuous assay: autoactivation of the enzyme is an intermolecular autophosphorylation process. *Biochemistry* **34**, 14843-14851 (1995).
75. R. T. Strachan *et al.*, Divergent Transducer-specific Molecular Efficacies Generate Biased Agonism at a G Protein-coupled Receptor (GPCR). *Journal of Biological Chemistry* **289**, 14211-14224 (2014).